Impact of light-absorbing particles on snow albedo darkening and associated radiative forcing over High Mountain Asia: High resolution WRF-Chem modeling and new satellite observations

Chandan Sarangi[1], Yun Qian[1*], Karl Rittger[2], Kat J. Bormann[3], Ying Liu[1], Hailong Wang[1], Hui Wan[1], Guangxing Lin[1], and Thomas H Painter[3]

[1]Pacific Northwest National Laboratory, Richland, WA

[2]Institute of Arctic and Alpine Research, Boulder, CO

[3]Jet Propulsion Laboratory, California Institute of Technology, Pasadena, CA

Submitted to the Atmospheric Chemistry and Physics

September 13, 2018

Corresponding Author: yun.qian@pnnl.gov

Abstract

Light-absorbing particles (LAPs), mainly dust and black carbon, can significantly impact snowmelt and regional water availability over High Mountain Asia (HMA). In this study, for the first time, online aerosol-snow interactions enabled and a fully coupled chemistry Weather Research and Forecasting (WRF-Chem) regional model is used to simulate LAP-induced radiative forcing on snow surfaces in HMA at relatively high spatial resolution (12 km, WRF-HR) than previous studies. Simulated macro- and micro-physical properties of the snowpack and LAP-induced snow darkening are evaluated against new spatially and temporally complete datasets of snow covered area, grain size, and impurities-induced albedo reduction over HMA. A WRF-Chem quasi-global simulation with the same configuration as WRF-HR but a coarser spatial resolution (1 degree, WRF-CR) is also used to illustrate the impact of spatial resolution on simulations of snow properties and aerosol distribution over HMA. Due to a more realistic representation of terrain slopes over HMA, the higher resolution model (WRF-HR) shows significantly better performance in simulating snow area cover, duration of snow cover, snow albedo and snow grain size over HMA, as well as an evidently better atmospheric aerosol loading and mean LAPs concentration in snow. However, the differences in albedo reduction from model and satellite retrievals is large during winter due to associated overestimation in simulated snow fraction. It is noteworthy that Himalayan snow cover have high magnitudes of LAP-induced snow albedo reduction (4-8 %) in pre-monsoon (both from WRF-HR and satellite estimates), which, induces a snow-mediated radiative forcing of ~ 30-50 W/m^2. As a result, Himalayas (specifically western Himalayas) hold the most vulnerable glaciers and mountain snowpack to the LAP-induced snow darkening effect within HMA. In summary, coarse spatial resolution and absence of snow-aerosol interactions over Himalaya cryosphere will result in significant underestimation of aerosol effect on snow melting and regional hydroclimate.

1. Introduction

Light-absorbing aerosol particles (LAPs; airborne dust and black carbon (BC) specks), can impact on regional water availability over Asia in three ways. Firstly, LAPs can directly interact with incoming solar radiation and induce thermo-dynamical modifications to synoptic scale circulations (Hansen et al., 1997 ; Ramanathan et al., 2001; Bond et al., 2013; Lau et al., 2006; Bollasina et al., 2011; Li et al., 2016). Secondly, acting as cloud condensation nuclei, changes in concentrations of these particles can lead to microphysical modification of cloud systems and precipitations (Fan et al., 2016; Li et al., 2016 ; Qian et al., 2009; Sarangi et al., 2017). Finally, deposition of LAPs in the snowpack can also darken the snow, reduce its surface albedo and accelerate snow warming and melting (Warren and Wiscombe, 1980; Qian et al., 2015; Qian et al., 2011; Qian et al., 2009a; Lau et al., 2010; Xu et al., 2009; Hadley and Kirchstetter, 2012; Dang et al., 2017). Modeling studies have suggested that the LAP-induced snow darkening mechanism has warming and snow-melting efficacy even greater than that of greenhouse gases (GHGs) (Hansen and Nazarenko, 2004; Flanner et al., 2007; Qian et al., 2011; Skiles et al., 2012). To give a perspective, the concentration of just 100 ng of BC in 1 g of snowpack will reduce the visible-wavelength albedo of grain radius 1000 μm by 10% (Fig. 1b of Warren, 2013). A chain of positive feedback mechanisms results in such large impact of LAPs (Qian et al., 2015). Initially, as snow starts to melt, the concentration of LAPs in snowpack increases because a portion of LAPs accumulate at the surface of the snowpack instead of getting washed away with meltwater (Conway et al., 1996; Flanner et al., 2007; Doherty et al., 2010). This increase in LAP concentration leads to enhanced warming of the snowpack and thereby increases the effective snow grain size, which further lowers snow albedo (Warren and Wiscombe, 1980; Hadley and

Kirchstetter, 2012). Nonetheless, at higher concentrations, grain sizes can again be reduced due to the loss of mass from surface layers with the intense melting (Painter et al., 2013). As this process continues, sufficient snow melt occurs to expose the darker underlying surface, leading to enhanced warming and snow ablation commonly-known as "snow albedo feedback" (Warren and Wiscombe, 1980; Hansen and Nazarenko, 2004; Flanner et al., 2007; Qian et al., 2015). In turn, this earlier loss of snow cover induces surface warming and perturbing regional circulations (Hansen and Nazarenko, 2004; Lau et al., 2010; Qian et al., 2011). This LAP-induced modification of snow albedo feedback is identified as one of major forcing agents affecting climate change with a high level of uncertainty (IPCC, 2013).

High Mountain Asia (HMA) includes the Tibetan plateau, central Asian mountains and the Himalaya cryosphere. It holds the largest glacial cover (~9500 glaciers) outside the polar region (Dyurgerov, 2001). Observations revealed that a historical decadal increase in the surface air temperature over HMA in a range of 0.6-1.8 ^{o}C (Shrestha et al., 1999;Wang et al., 2008), and the warming is faster over higher elevations (> 4000 m) in the last three decades (Xu et al., 2009b; Ghatak et al., 2014). The Himalaya glacier area has cumulatively decreased by ~16% during the period 1962 to 2004 (Kulkarni et al., 2010) and the pre-monsoon snow cover is decreasing at a decadal rate of ~0.8 million km^2 during the last 50 years (Brown and Robinson, 2011). The average retreat rate on the north slope of Mount Everest is as high as 5.5–9.5 m y^{-1} (Ren et al., 2006). The Himalaya cryosphere contributes to the stream flow in Indus and Ganges river systems by ~ 50 % and ~10-30%, respectively (Khan et al., 2017). Warming and glacier retreat over the Himalaya cryosphere have a great potential to impact the fresh water availability for about 700 million people, modify regional hydrology, and disturb the agrarian

economy of all South Asian countries (Bolch et al., 2012;Immerzeel et al., 2010;Kaser et al., 2010;Singh and Bengtsson, 2004;Barnett et al., 2005;Yao et al., 2007). Therefore, it is critical to disentangle the factors contributing to glacier retreat and snow melt over HMA.

Regional warming due to increasing greenhouse gases (Ren and Karoly, 2006) has been reported as the primary cause of the high rate of warming and glacier retreat over HMA. However, in the last decade, advancement in remote sensing and availability of measurements from several field campaigns suggest that the contribution of LAP loading (in the atmosphere) to the warming and glacier melting over HMA is probably greater than previously believed (Ramanathan et al., 2007; Prasad et al., 2009; Menon et al., 2010). Continuous observations over the Nepal Climate Observatory Pyramid (NCO-P) facility located at 5079 m a.s.l. in the southern foothills of Mt. Everest revealed very high concentrations of black carbon (Marcq et al., 2010) and desert dust (Bonasoni et al., 2010) especially in pre-monsoon from Indo-Gangetic plains. Atmospheric LAPs are scavenged to the snow/ice surface by dry and wet deposition and cause measurable snow darkening and melting (Gautam et al., 2013; Yasunari et al., 2010b;Yasunari et al., 2013; Nair et al., 2013; Ménégoz et al., 2014; Ming et al., 2008;Flanner and Zender, 2005). Thus, LAP deposited in snow and associated snow darkening has been suggested as a key factor to the early snowmelt and rapid glacier retreat over HMA (Yasunari et al., 2010; Ming et al., 2008; Xu et al., 2009a; Flanner et al., 2007; Qian et al., 2011).

While previous studies have underlined the significance of LAP-deposition in snow over HMA, the estimation of LAP-induced snow darkening and associated radiative forcing is still highly uncertain (Qian et al., 2015). Many of these studies used online global model simulations at coarse spatial resolutions of ~50-150 km (Flanner and Zender, 2005; Ming et al., 2008; Qian et

al., 2011; Kopacz et al., 2011; Zhang et al., 2015). Other studies employed offline simulation of the snow albedo effect using measured or modelled concentrations of deposited LAP in surface snow or estimated from atmospheric loading and ice cores (Yasunari et al., 2013; Nair et al., 2013; Wang et al., 2015; He et al., 2014; Santra et al., 2019;Thind et al., 2019). The complex terrain of HMA, seasonal snowfall and near surface air circulation are not well resolved by coarse global climate models (Kopacz et al., 2011; Ménégoz et al., 2014). Similarly, offline estimations are limited in scope because they are site specific and are based on simplified assumptions about deposition rates. Ideally, online high resolution simulations allowing for LAP-snow interactions should facilitate a more realistic understanding of LAP deposition to snow and LAP-induced snow darkening effect in terms of both magnitude and spatial variability over HMA.

In this study, a modified version of the online chemistry coupled with Weather Research and Forecasting regional model (WRF-Chem v3.5.1), which, is then fully coupled with SNICAR (SNow, ICe, and Aerosol Radiative) model, is used to perform first-ever high resolution (12 km) simulation over the HMA region for the water year 2013-14 (October 1, 2013 to September 30, 2014). Satellite observations of snow properties like snow albedo, grain size, and LAP-induced snow darkening from MODSCAG and MODDRFS retrievals are used for evaluation (Painter et al, 2009; 2012). The main objective of this study is to evaluate the skill of high resolution WRF-Chem model in simulating properties of snowpack, aerosol distribution, LAP in snow and LAP-induced snow darkening over HMA using spatially and temporally complete (STC) remotely sensed snow surface properties (SSP) from MODIS (Dozier et al, 2008; Rittger et al, 2016). Our second objective is to demonstrate the benefit for aerosol and snow distributions in high

resolution runs by comparing to a coarse gridded quasi-global model simulation over HMA. This quasi-global simulation is run with the same WRF-Chem configuration but at 1 degree spatial resolution. Finally, the spatiotemporal variation of simulated LAP deposition, snow albedo darkening and snow mediated LAP radiative forcing (LAPRF) over HMA are discussed. The model details and datasets used are described in Section 2. Results and discussions are presented in Section 3 followed by conclusions in Section 4.

2: Model simulations and observational datasets

Below, we provide details on the aerosol module used in WRF-Chem, interactive coupling with aerosol and SNICAR via land model, and the model setup for both 12 km and 1 degree resolution runs. The details for the remote sensing observations that are used to evaluate the models are also provided.

2.1: Coupled WRF-Chem-CLM-SNICAR Model description

The WRF-Chem simulation is performed at 12 km × 12 km horizontal resolution (hereafter refereed as WRF-HR) with 210 × 150 grid cells (64–89°E, 23–40°N) (Figure 1) and 35 vertical layers. The simulation was conducted from 20th September, 2013 to 30th September, 2014, to provide one year of results (following a 10-day model spin-up). ERA-interim reanalysis data at 0.7° horizontal resolution and 6 h temporal intervals are used for meteorological initial and lateral boundary conditions. The simulation is re-initialized every 4th day to prevent the drift of model meteorology. Model physics options used are the MYJ (Mellor–Yamada– Janjic) planetary boundary layer scheme, Morrison 2-moment microphysics scheme, community land

model (CLM), Kain-Fritsch cumulus scheme and Rapid Radiative Transfer Model for GCMs (RRTMG) for longwave and shortwave radiation schemes.

The CBM-Z (carbon bond mechanism) photochemical mechanism (Zaveri and Peters, 1999) coupled with eight bin MOSAIC (Model for Simulating Aerosol Interactions and Chemistry) aerosol model (Zaveri et al., 2008) is used. This is the most sophisticated aerosol module available for the WRF-Chem model. The sectional approach with eight discrete size bins is used to represent the size distributions of all the major aerosol components (including sulfate, nitrate, ammonium, black carbon (BC), organic carbon (OC), sea salt, and mineral dust) in the model. The processes of nucleation, condensation, coagulation, aqueous phase chemistry, and water uptake by aerosols in each bin size are included in the MOSAIC module. Dry deposition of aerosol mass and number is simulated by including both diffusion and gravitational effects as per Binkowski and Shankar (1995). Wet removal of aerosols follow Easter et al. (2004) and Chapman et al. (2009) and includes grid resolved impaction and interception processes for both in-cloud (rainout) and below-cloud (washout) aerosol removal. Processes involved in convective transport and wet removal of aerosols by cumulus clouds are described in Zhao et al. (2013).

Anthropogenic emissions used in our study is at $0.5^{O} \times 0.5^{O}$ horizontal resolution and are taken from the NASA INTEX-B mission Asian emission inventory for year 2006 (Zhang et al., 2009). Biomass burning emissions at $0.5^{\circ} \times 0.5^{\circ}$ horizontal resolution for the water year 2013-14 are obtained from the Global Fire Emissions Database, Version 3 (GFEDv3) (Van Der Werf et al., 2010), which are vertically distributed in our simulation using the injection heights prescribed by Dentener et al. (2006) for the Aerosol Inter Comparison project (AeroCom). Sea

salt and dust emissions follow Zhao et al. (2014). Dust surface emission fluxes are calculated with the Georgia Institute of Technology-Goddard Global Ozone Chemistry Aerosol Radiation and Transport (GOCART) dust emission scheme (Ginoux et al., 2001), and emitted into the eight MOSAIC size bins with respective mass fractions of 10^{-6} , 10^{-4} , 0.02, 0.2, 1.5, 6, 26, and 45%.

Aerosol optical properties are computed as a function of wavelength for each model grid cell. The Optical Properties of Aerosols and Clouds (OPAC) data set (Hess et al., 1998) is used for the shortwave (SW) and longwave (LW) refractive indices of aerosols and a complex refractive index of aerosols (assuming internal mixture) is calculated by volume averaging for each chemical constituent of aerosols for each bin. A spectrally-invariant value of 1.53 ± 0.003i is used for the SW complex refractive index of dust. Fast et al. (2006) and Barnard et al. (2010) provide detailed descriptions of the computation of aerosol optical properties such as extinction coefficient, single scattering albedo (SSA), and asymmetry factor in WRF-Chem. Following Zhao et al. (2011) and Zhao et al. (2013a), aerosol radiative feedback is coupled with the Rapid Radiative Transfer Model (RRTMG) (Mlawer et al., 1997) and the direct radiative forcing of individual aerosol species in the atmosphere are diagnosed. Aerosol–cloud interactions are included in the model following Gustafson et al. (2007).

The increasingly used Snow, Ice, and Aerosol Radiation (SNICAR) model simulates the snow properties and associated radiative heating rates of multilayer snow packs (Flanner and Zender, 2005; Flanner et al., 2009, 2012 and 2007). Fundamentally, it employs the snow albedo theory (parameterization) based on Warren and Wiscombe (1980) and the two-stream radiative approximation for multilayers from Toon et al. (1989). SNICAR can also simulate aerosol radiative effect in snow for studying the LAP heating and snow aging (Flanner et al., 2007).

Recently, laboratory and site measurements are used to validate the SNICAR simulated change of snow albedo for a given BC concentration in snow (Hadley and Kirchstetter, 2012; Brandt et al., 2011). For radiative transfer calculations, SNICAR defines layers matching with the five thermal layers in community land model (CLM) that vertically resolve the snow densification and meltwater transport (Oleson et al., 2010). Note that the number of snow layers and thickness of top snow surface layer are predicted in the CLM model. Fresh snowfall and melting continuously affect the model surface snow layer thickness (3 cm or less). Therefore, LAP concentrations within each snow layer depend on meltwater flushing, new snowfall and associated top layer evolution (Flanner et al., 2007, 2012; Oleson et al., 2010). In WRF-Chem-SNICAR coupled model, BC and dust deposition on snow is calculated in a prognostic approach through dry and wet deposition processes. BC in snow can be represented as externally and internally mixed with precipitation hydrometeors depending on the removal mechanism involved, but dust is considered to only mix externally with snow grains (following Flanner et al., 2012). SNICAR in WRF-Chem simulates four tracers of dust based on size (with diameters of 0.1–1, 1–2.5, 2.5–5, and 5–10 μm) and two tracers of BC (externally and internally mixed BC with 0.2 μm dry diameter) in snow. The MOSAIC aerosol model simulates dust in the atmosphere with eight size bins (0.039–0.078, 0.078–0.156, 0.156–0.312, 0.312–0.625, 0.625 - 1.25, 1.25–2.5, 2.5–5.0, and 5.0–10.0 μm in dry diameter). The first 4 bins are coupled with the smallest bin of dust particles in SNICAR. While the next two MOSAIC bins (5^{th} and 6^{th}) map into the second bin of SNICAR, the 7^{th} and 8^{th} MOSAIC dust bins correspond to the third and fourth SNICAR dust bins (Zhao et al., 2014), respectively. Deposition of LAPs to snow in SNICAR are immediately mixed in the CLM surface snow layer (< 3 cm). CLM adds excess water in the layer

above to the layer beneath during melting. The scavenging of aerosols in snow by meltwater is assumed to be proportional to its mass mixing ratio of the meltwater multiplied by a scavenging factor. Scavenging factors for externally mixed BC and internally mixed BC are assumed to be 0.03 and 0.2, respectively, and 0.02, 0.02, 0.01, and 0.01 for the four dust bins (all externally mixed). Although these scavenging factors are comparable to observations (Doherty et al., 2013), the scavenging ratios can be highly heterogeneous and introduce high uncertainty into the estimation of LAP concentrations in snow (Flanner et al., 2012; Qian et al., 2014). More detailed description about the aerosol deposition and mixing processes, computation of optical properties of snow and LAPs in WRF-Chem-CLM-SNICAR coupling can be found in Zhao et al.(2014) and Flanner et al.(2012).

Configured in the way similar to the WRF-HR, a coarse (1° × 1°) gridded WRF-Chem simulation is also performed using a quasi-global model (hereafter referred as WRF-CR) with 360 × 130 grid cells (180° W–180° E, 60° S–70° N). Periodic boundary conditions are used in the zonal direction. Reanalysis of the TROpospheric (RETRO) anthropogenic emissions for the year 2010 (ftp://ftp.retro.enes.org/ pub/emissions/aggregated/anthro/0.5x0.5/) is used for anthropogenic aerosol and precursor gas emissions in the coarse gridded quasi-global WRF-Chem simulation except for Asia and the United States. INTEX-B anthropogenic emissions (Zhang et al., 2009) and US National Emission Inventory are used for Asia and the U.S., respectively. Emissions of biomass burning aerosols, sea salt, and dust are treated in the same way as described above for the WRF-HR simulation. More details about the quasi-global WRF-Chem simulation can be found in (Zhao et al., 2013b);Hu et al., 2016). Chemical initial and

boundary conditions to the WRF-HR simulation are provided by this quasi-global WRF-CR runs for the same time period to include long-range transported chemical species.

2.2: Aerosol Optical Depth (AOD) dataset

The aerosol robotic network (AERONET – https://aeronet.gsfc.nasa.gov) is a global network of ground based remote sensing stations that provides quality-controlled measurements of AOD with uncertainties ~0.01 under clearsky conditions over India (Holben et al., 1998; Dubovik et al., 2000). CIMEL Sun scanning spectral radiometers are used to measure direct Sun radiance at eight spectral channels (340, 380, 440, 500, 675, 870, 940, and 1020 nm) and measure spectral columnar AOD (Holben et al., 1998). AERONET provides measurements at ~15 min temporal resolution from sunrise to sunset.

Skyradiometer Network (Skynet) is another global network of ground based spectral scanning radiometer (POM-01L, Prede, Japan) stations that provides quality-controlled measurements of AOD (Nakajima et al., 1996). With an automatic sun scanner and sensor, it measures sky irradiance in five wavelengths i.e. 400, 500, 675, 870, and 1020 nm. The measured monochromatic irradiance data is processed by using Skyrad.Pack version 4.2 software. Calibration of the Sky radiometer is carried out on a monthly basis (http://atmos3.cr.chiba-u.jp/skynet/data.html). Details of the instrumentation and software protocol can be found in Campanelli et al. (2007) and Ningombam et al., (2015). In this study, we have also used AOD measurements at 500 nm over MERAK, a high altitude Skynet station in Himalaya for water year 2013-14.

The MODerate resolution Imaging SpectroRadiometer (MODIS) instrument onboard the NASA AQUA satellite provides global coverage of daily radiance observations (at 1330 LT) in 36 spectral channels. Over North India, Tripathi et al., (2005) has shown that MODIS observations correlate well with ground based measurements. For the evaluation of model simulated AOD, 1° gridded Level 3 AOD estimates (collection 6) at 0.55 μm wavelength obtained from the MODIS instrument are used during water year 2013-14. However, the MODIS land aerosol algorithm uses a dark target approach (Levy et al., 2007), which, is known to have large uncertainties over arid and mountainous surfaces (Levy et al., 2010).

2.3: Spatially and temporally complete MODSCAG and MODDRFS retrievals

Subpixel snow-covered area and snow grain size are retrieved from MODIS-observed surface reflectance data using the physically based MODIS Snow-Covered Area and Grain size (MODSCAG) (Painter et al., 2009) algorithm. In each snow covered pixel, MODSCAG attributes a fractional snow-covered area and grain size using spectral mixture analysis to determine proportion of the pixel that is snow and is not snow. MODSCAG is more accurately identifies snow cover throughout the year than the widely used MODIS snow product: MOD10A1 (Rittger et al., 2013). The MODSCAG snow-mapping algorithm for fraction of snow covered area has an uncertainty of ~ 5 % (Rittger et al., 2013). The current study incorporates pixel level snow cover area and snow grain size from MODSCAG over the HMA region to evaluate snow pack simulation and LAP-induced albedo reduction. Further, MODIS Dust Radiative Forcing in Snow (MODDRFS) model (Painter et al., 2012) is used to determine the LAP-induced albedo reduction over HMA. MODDRFS uses spectral reflectance differences between the measured snow spectral albedo and the modeled clean snow spectral albedo. The pixel level clean snow

spectrum corresponding to MODSCAG retrieved snow grain sizes is calculated using discrete ordinate radiative transfer solutions for visible wavelengths and solar zenith angles. Coupled, these products provide the determination of snow albedo for the fractional snow cover with LAP inclusion.

Reflectance inputs to MODSCAG and MODDRFS are degraded by cloud cover, off-nadir views, and data errors, but can be filtered in time and space to improve data quality and consistency. Our method for spatially cleaning and filling (Dozier et al., 2008;Rittger et al., 2016) combines noise filtering, snow/cloud interpolation and smoothing to improve the daily estimates snow surface properties (SSP). Using remotely sensed forest height maps (Simard et al., 2011) and MODSCAG vegetation fraction, we adjust the satellite viewable snow cover to account for snow under tree canopy (Rittger et al., 2016). We weight the observations based on satellite viewing angle that varies from 0 to 65 degree with larger uncertainties in off-nadir views (Dozier et al., 2008). The result is a set of spatially and temporally complete (STC) SSPs. Use of these products in an energy balance model to estimate snow water equivalent based on reconstruction produced more accurate snow cover than the Snow Data Assimilation System (SNODAS) or an interpolation of observations from snow pillows (Bair et al., 2016). In this study we use STC versions of MODSCAG and MODDRFS when comparing our WRF model output. The incomplete remotely sensed would be difficult to use given the gaps in data and uncertainties related to viewing angle (Dozier et al., 2008). Hereafter, the use of MODSCAG and MODDRFS terms will invariably refer to these STC-MODSCAG and STC-MODDRFS products.

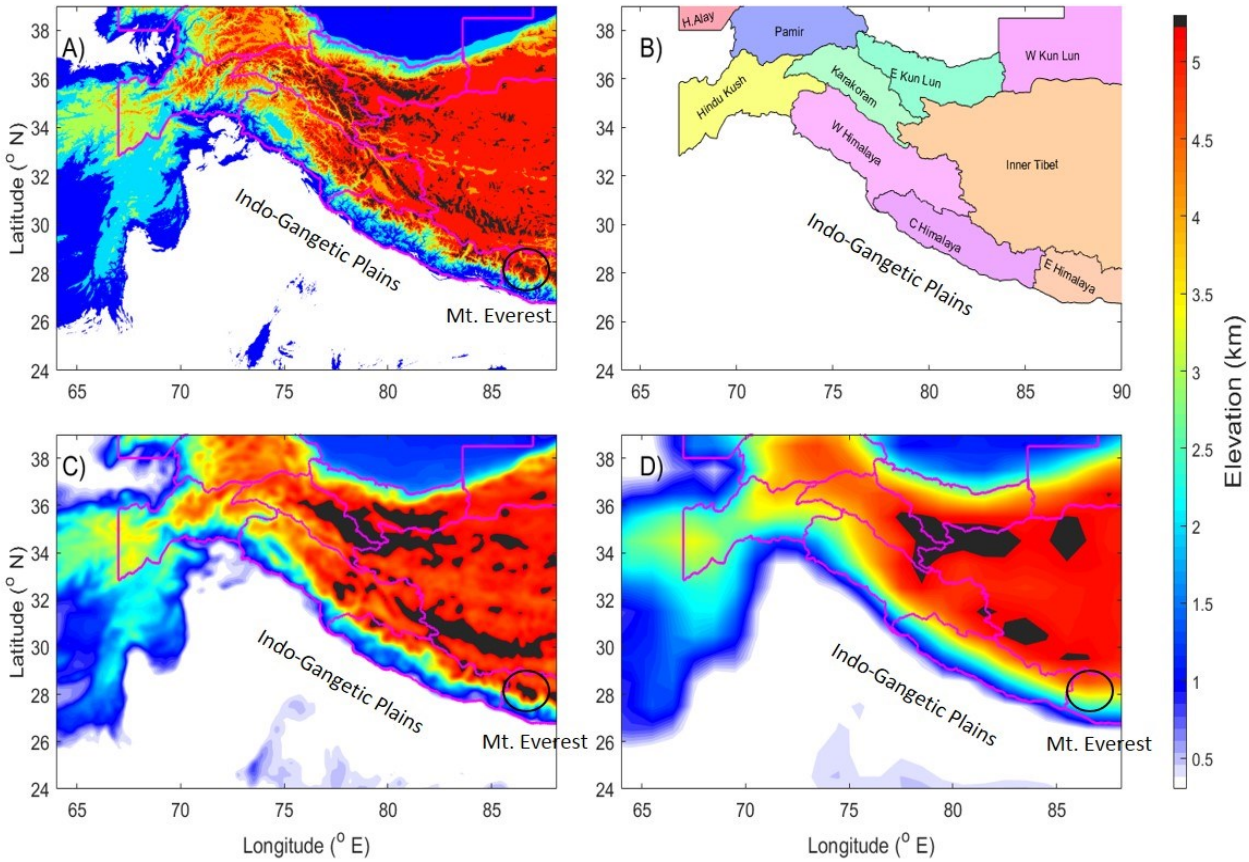

Figure 1: Panel A illustrates the terrain elevation at 1 km resolution from ETOPO1 dataset. Panel B shows glacier classification over HMA region used in this study following Randolph Glacier Inventory. Panels C and D illustrate terrain representation in WRF-HR run (12 km) and WRF-CR (1 degree) runs, respectively. For reference, Mt. Everest (shown as black circle in Figure 1C) is distinctly represented in Panel A and C, but not in Panel B.

2.4: Variation in terrain representation in WRF-HR and WRF-CR

Figure 1A illustrates the variations in terrain height over HMA at a resolution of 1 arc using ETOPO1 Global Relief Model, a publicly available global topographical dataset (Amante and Eakins, 2009). It clearly shows the enormous relief in terrain as we move from the Indo Gangetic plains (IGP) to the crest of the Himalaya and into the Tibetan Plateau (TP). The majority of HMA is above 4 km altitude with many Himalaya peaks at an altitude higher than 6

km. Figure 1B illustrates the mountain ranges and glaciers classified as per the Randolph Glacier Inventory in the Fifth Assessment Report of the Intergovernmental Panel on Climate Change (Pfeffer et al., 2014). Specifically, Pamirs, Hindu Kush, Karakoram, Kunlun, and Himalaya hold the most number of glaciers in HMA. Figures 1C and 1D illustrate the representation of terrain elevation in WRF-HR and WRF-CR, respectively. Compared to Figure 1A, location of mountain peaks (altitude > 5.5 km) are better represented in WRF-HR compared to WRF-CR, as is particularly evident over the Karakoram, Kunlun, and Himalaya ranges. Moreover, the steep rise in elevation between IGP and TP is also well represented by WRF-HR, whereas it is more gradual in WRF-CR.

2.5: Methodology

Simulation of the snow macro- and micro-physical properties, aerosol loading and LAP in snow concentration from WRF-HR, WRF-CR and observational estimates (datasets described above) over HMA are compared in Section 3.1 and Section 3.2. In Section 3.3, the WRF-HR simulated LAP-induced snow albedo reduction values over HMA is compared with corresponding MODIS satellite based STC-MODSCAG and STC-MODDRFS. Lastly, a discussion on the high resolution model simulated LAP-induced radiative forcing estimates over HMA is also presented in context to previous studies and other atmospheric forcing.

The simulated fractional snow covered area (fSCA), duration of snow cover over a grid in terms of number of snow cover days (NSD), snow albedo (α) and snow grain sizes (SGS) and LAP-induced snow albedo darkening ($\Delta\alpha$) for midday (1000 -1400 LT) conditions from both the WRF models are compared with corresponding STC-MODSCAG and STC-MODDRFS retrievals

over HMA. The number of snow cover days (NSD: defined as days having fSCA values ≥ 0.01) during water year 2013-14 is determined over each grid from STC-MODSCAG and both model runs. They are compared with corresponding values from STC-MODSCAG retrievals, which, are observed during Terra overpasses at 10:30 LT. We have used a window from 10:00 LT to 14:00 LT for representing midday averages of modelled variables to incorporate the variability due to differences in timing (between model and real scenario) of weather conditions like precipitation and clouds. In addition, the change in snow albedo during 10:00 - 14:00 LT is < 0.01 (Bair et al., 2017), which, is low compared to other model physics- and data retrieval related uncertainties. The WRF-CR simulated variables and STC-MODSCAG and STC-MODDRFS retrievals are gridded to the resolution of WRF-HR (12 km) for ease of comparison. We have compared annual mean values as well as seasonal mean values for winter (December - February) and pre-monsoon (April - June) season, separately. We have not considered the monsoon period in our analyses because the snow cover during the monsoon is negligible (except in glaciated regions at high altitudes) relative to other months (Figure S1). Simulated SGS values only from the topmost snow surface layer is compared to the MODSCAG SGS retrievals. To evaluate spatial heterogeneity in our model, the seasonal and annual distribution of these variables are calculated separately for each sub region (shown in Figure 1) within HMA. In addition, to gain an understanding of the extent of temporal variability present in LAP-induced effects, we have also presented daily midday variation in LAP-induced snow darkening and LAP-induced radiative forcing at surface over Chotta Shingri glacier region (32.1-32.35 ^{o}N, 77.4-77.7 ^{o}E) located in the Chandra–Bhaga river basin of Lahaul valley, Pir Panjal range, in Western Himalayas. It is an accessible and representative site for glacier mass balance studies in western

Himalayas. Chotta Shigri glacier has a cumulative glaciological mass loss of –6.72 m w.e. between 2002 and 2014 (Azam et al., 2016).

The simulated aerosol optical depth (AOD) is compared with available in-situ observations (described in Section 2.2). Here, quality assured (Level 2) midday (1000 to 1400 LT) averages of AOD (550 nm) at seven AERONET stations (Lahore, Jaipur, Kanpur, Gandhi college, Kathmandu and CAS) and one SkyNet site within our study region are used to evaluate the simulated AOD values. Further, the simulated distribution of LAP concentration in snow at a few sites is compared with field measurements. Only a few field measurements of concentration of BC (LAP_{BC}) and dust particles (LAP_{dust}) in the snow surface or the surface layer are available over glaciated regions within our study domain. In this study, measurements of LAP_{BC} over Muztagh Ata in eastern slopes of Pamirs (Xu et al., 2006), Uttaranchal region of W. Himalayas (Svensson et al., 2018), East Rongbuk at 6.4 km altitude (Ming et al., 2012; Ming et al., 2008; Xu et al., 2009a) and composite of recent in-situ measurements from various studies near the NCO-pyramid site in Nepal at 5-6 km altitude (Kaspari et al., 2014; Yasunari et al., 2013; Jacobi et al., 2015; Ginot et al., 2014) is used. We have used more than one study to have a range of annual mean LAP values over each location so in principle the observations are representative of different years and different snow depths over the same glacier. Moreover, simulated annual mean LAP concentration only from the topmost snow surface layer is compared to the observed surface snow LAP in snow concentration, which introduce differences in the snow sample depth used for the evaluation. However, to minimize the influence of snow sample depth variation, we have only used data in the literature which are observed as snow surface measurement or from snow pits having a thickness less than 15 cm. Similarly, the point

measurements used for evaluating LAP_{dust} are over Abramov glacier in western slopes of Pamirs (Schmale et al., 2017), Muztagh Ata in eastern slopes of Pamirs (Wake et al., 1994) , East Rongbuk (Ming et al., 2012) and near NCO-pyramid station (Ginot et al., 2014), respectively.

3: Results and Discussions

3.1: Snow physical, microphysical and optical properties

The largest values of region-averaged annual mean fSCA within HMA are observed in both the satellite retrievals and the model runs over the Karakoram region (mean=0.45) followed by Pamirs, Himalayas and Hindu Kush in the HMA region (Figures 2A and 2B). In comparison, the fSCA over Kunlun and TP are lower (<0.3), but, pockets of very high fSCA (~0.7) are visible over the west Kunlun ranges (Figure 2A). The annual mean fSCA values and the fine spatial variability are well simulated by WRF-HR (Figure 2B) over the entire HMA region. Of exception are simulations over the Karakoram, where WRF-HR overestimates annual mean fSCA, however, the distribution of annual mean fSCA from WRF-HR and STC-MODSCAG agree in all the sub regions (Figure 2D). This observation is largely valid also for pre-monsoon months (Figure 2F). But, significant overestimation in distribution of fSCA (by >0.2) during winter is present over Pamirs, Karakoram, W. Himalayas, TP and Kunlun region (Figures 2E). STC-MODSCAG retrievals illustrate that the Pamirs (NSD=230 days) and Karakoram (NSD=270 days) ranges remain snow covered for 7-9 months of the year (Figure 3A). Similarly, the grids in Hindu Kush (NSD=194), W. Himalayas (NSD=189 days) and C. Himalayas (NSD=191 days) are snow covered for ~ 6-7 months. Mountains in E. Himalayas (NSD=142 days) remain snow covered for only 4-5 months

of the year. The distribution of annual NSD values simulated by WRF-HR in each sub region is close to STC-MODSCAG values (Figure 3D). Also, the spatial distribution and magnitude of simulated NSD by WRF-HR is similar to that from STC-MODSCAG for different seasons, separately (Figure S2). Thus, overestimation of annual mean fSCA in WRF-HR during winter is not due to mere averaging error associated with underestimation in simulated NSD during winter (Figure S2).

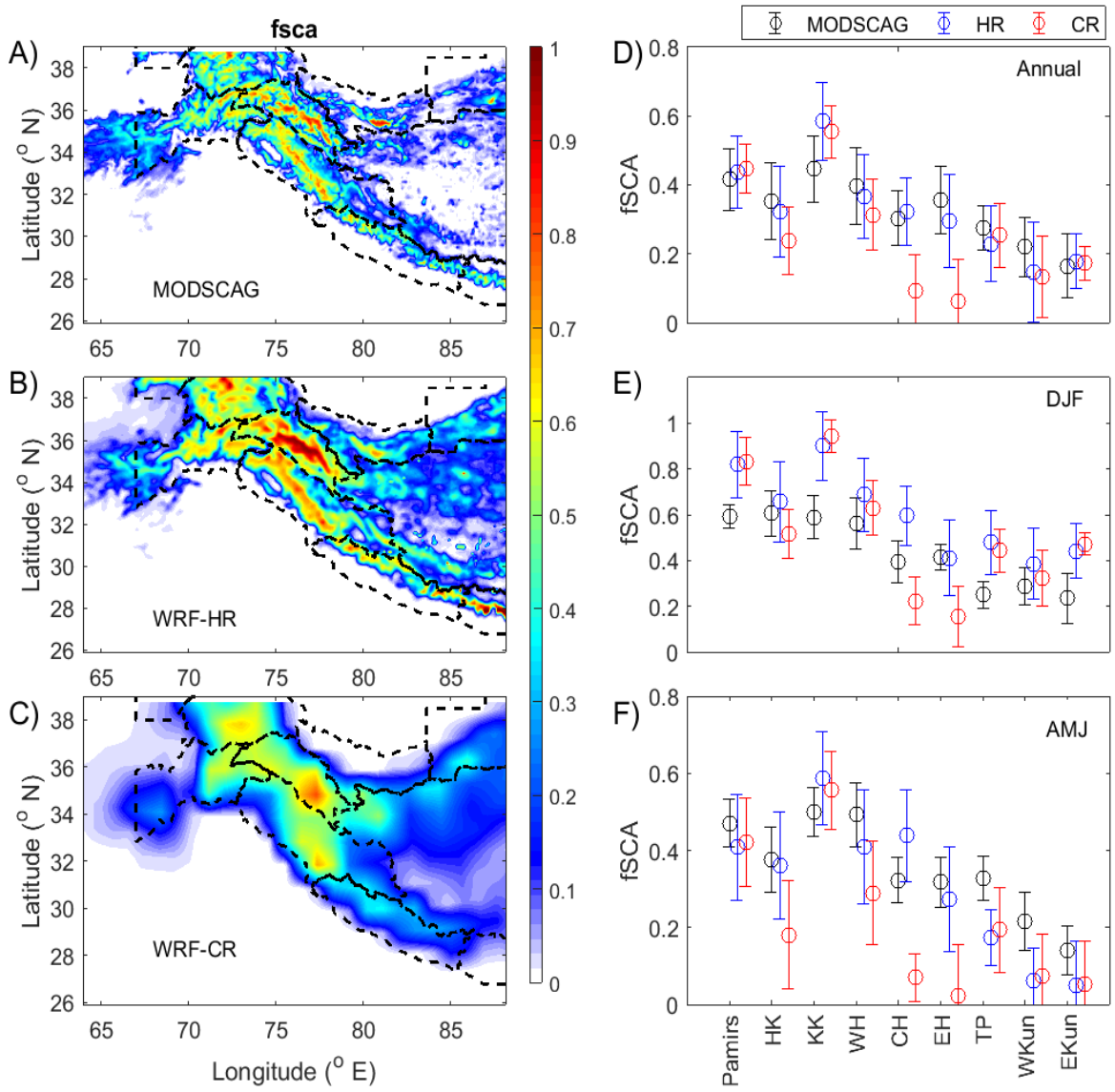

Figure 2: Spatial distribution of annual mean snow cover fraction (fSCA) during midday (1000-1400 LT) for water year 2013-14 from A) STC-MODSCAG retrievals, B) simulated values from WRF-HR and C) WRF-CR simulations. Panels D-F illustrate the distribution of midday mean fSCA over each subregion identified by glacier classification following Randolph Glacier Inventory (X-axis). The circle and vertical legs represent mean±standard deviation over each region for D) entire year, E) winter (December - February) and F) pre-monsoon (April - June) season, separately. Here, Hindu Kush, Karakoram, W.Himalayas, C.Himalayas, E.Himalayas, Tibetan Plateau, West Kunlun and East Kunlun regions are abbreviated as HK, KK, WH, CH, EH, TP, WKun and EKun, respectively.

We also calculated the number of days of snow cover with low fSCA (<0.5; Figure 3B) and high fSCA (>0.5; Figure 3C) values, separately. The grids in Kunlun, Northern slope of Karakoram, eastern slope of Pamirs and TP region are dominated by snow cover of relatively low fSCA for most of their snow cover duration (Figure 3B). But, grids in Hindu Kush, Himalayas and southern slopes of Karakoram are generally covered with high fSCA values throughout the year (Figure 3C). The distribution of simulated NSD values over each sub region for low and high fSCA scenario is shown in Figures 3E and 3F, respectively. WRF-HR can well simulate the NSD over grids with high fSCA (Figure 3F) but significantly underestimates NSD over grids with low snow cover (Figure 3E). Note that the regions dominated by low annual fSCA in this water year are actually the same regions where WRF-HR simulated fSCA values are being overestimated in winter (Figure 2E). Thus, simulation of fewer number of days with low fSCA (and vice versa) in WRF-HR might also be contributing partially to the overestimation of winter fSCA simulated in WRF-HR compared to STC-MODSCAG. Further, WRF-HR simulated annual surface rainfall in winter is overestimated over Karakoram, Himalayan and Hindukush ranges (Figure S3). This indicates that overestimation of surface precipitation in WRF-HR may also contribute to the overestimation of fSCA over HMA in winter. Interestingly, WRF-CR simulated NSD values for low fSCA case is also in better agreement with STC-MODSCAG values (Figure 3E). Winter mean distribution of WRF-CR simulated fSCA over Kunlun, W.Himalaya and TP region better match STC-MODSCAG values than the corresponding WRF-HR simulated fSCA values (Figure 2F). It is noteworthy that these subregions (which are dominated by low fSCA grids) receive snowfall from western disturbances during winter months. The cloud cover associated with the western disturbances over these sub regions are extensive in winter which also introduces uncertainty

in MODSCAG retrievals and STC processing and contributes to the differences between WRF-HR and MODSCAG in fSCA.

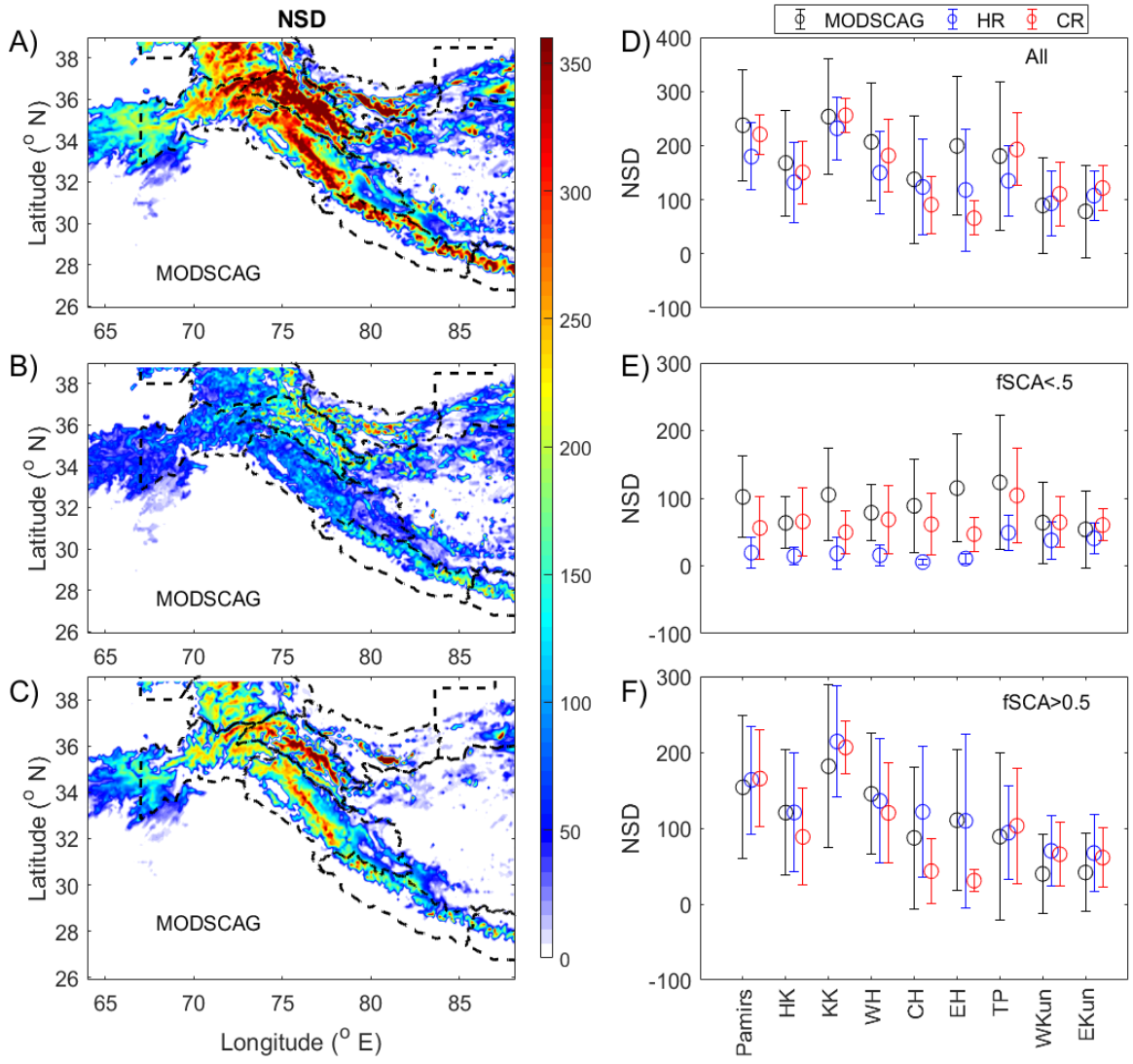

Figure 3: Spatial distribution of snow duration in terms of NSD from A) STC-MODSCAG retrievals. Panel B and C are similar to Panel A, but, shows number of days when fSCA is below and above 0.5 over each grid, respectively. Panels D illustrate the distribution of NSD over each sub region identified by glacier classification following Randolph Glacier Inventory. The circle and vertical legs represent mean ± standard deviation over each region for entire year. Here, Hindu Kush, Karakoram, W.Himalayas, C.Himalayas, E.Himalayas, Tibetan Plateau, West Kunlun and East Kunlun regions are abbreviated as HK, KK, WH, CH, EH, TP, WKun and EKun,

respectively. Panel E and F are similar to Panel D, but, for NSD corresponding to fSCA values below and above 0.5, respectively.

Comparison between performance of WRF-CR and WRF-HR for fSCA clearly show significant improvements in the WRF-HR simulations over the Hindu Kush and Himalayan ranges (Figure 2D). For instance, the simulated annual mean fSCA in WRF-CR around Mt. Everest (shown as black circle in Figure 1) is less than 0.1 (Figure 2C). This is contrary to the high fSCA values observed at Mt. Everest (0.7 in Figures 2A) and simulated by WRF-HR (0.7 in Figures 2B). Moreover, the improvement is present in both winter and pre-monsoon months indicating it's independence from meteorological variations (Figures 2E and 2F). Analysis of NSD values indicate that the snow cover duration in WRF-HR also improved significantly over these slopes (Figure S4) irrespective of the season. Note that WRF-CR underestimates the snow duration over Hindu Kush and Himalayas by ~2-6 months (Figure S4) and the spatial location of grids with very high annual mean fSCA values (mountain ranges) improved in WRF-HR compared to the STC-MODSCAG data (Figures 2A-C). The observed improvement in fSCA and NSD simulation over the slopes of Himalaya and Hindu Kush can be attributed to better terrain representation in WRF-HR.

Next, the simulated microphysical properties of the snow pack are evaluated against the remote sensing retrievals. Spatial patterns in annual mean SGS from STC-MODSCAG are similar to that seen in fSCA with highest values over the Karakoram and Himalayan ranges (Figures 4A) corresponding to the highest elevations and likely the coldest temperatures hindering snow grain growth. This spatial distribution of annual mean SGS values is well simulated in WRF-HR

runs (Figure 4B). But, the annual mean values over each subregion are largely overestimated by 30-50 micron (Figure 4D) relative to STC-MODSCAG. The seasonal distribution of region-segregated SGS values from WRF-HR also compares well with that from STC-MODSCAG retrievals (Figure 4E). Simulated annual mean SGS from WRF-CR (Figure 4C) lack the fine spatial variability seen in STC-MODSCAG and WRF-HR. Moreover, the SGS estimates are largely underestimated (by up to 100 microns) by WRF-CR specifically over grids in central and eastern Himalayas, TP and Kunlun ranges (Figure 4D). The large underestimation of SGS from WRF-CR and overestimation of SGS from WRF-HR is present for both pre-monsoon and winter months (not shown). The overestimation of SGS from WRF-HR values corroborate well with the finding that the simulated fSCA distribution from WRF-HR is largely skewed towards higher values (Figure 3). Similarly, the unrealistically low mean values of SGS from WRF-CR over Himalayas, TP and Kunlun ranges are consistent with the underestimation of fSCA and NSD values over these regions (Figure 2 and 3). While, SGS retrievals from STC-MODSCAG are based on observed surface reflectance, the modeled SGS is calculated from simulated snow mass in top model layer in the grid. Hence, improvement in simulation of fSCA and NSD in high resolution WRF-HR runs also caused the SGS values from WRF-HR to be closer to STC-MODSCAG retrievals than SGS from WRF-CR runs. It is worth noting that the presence of cloud cover influences STC-MODSCAG retrievals of SGS towards smaller grain sizes if clouds are misidentified as snow. This systematic error could also contribute to the SGS differences between WRF-HR and STC-MODSCAG estimates.

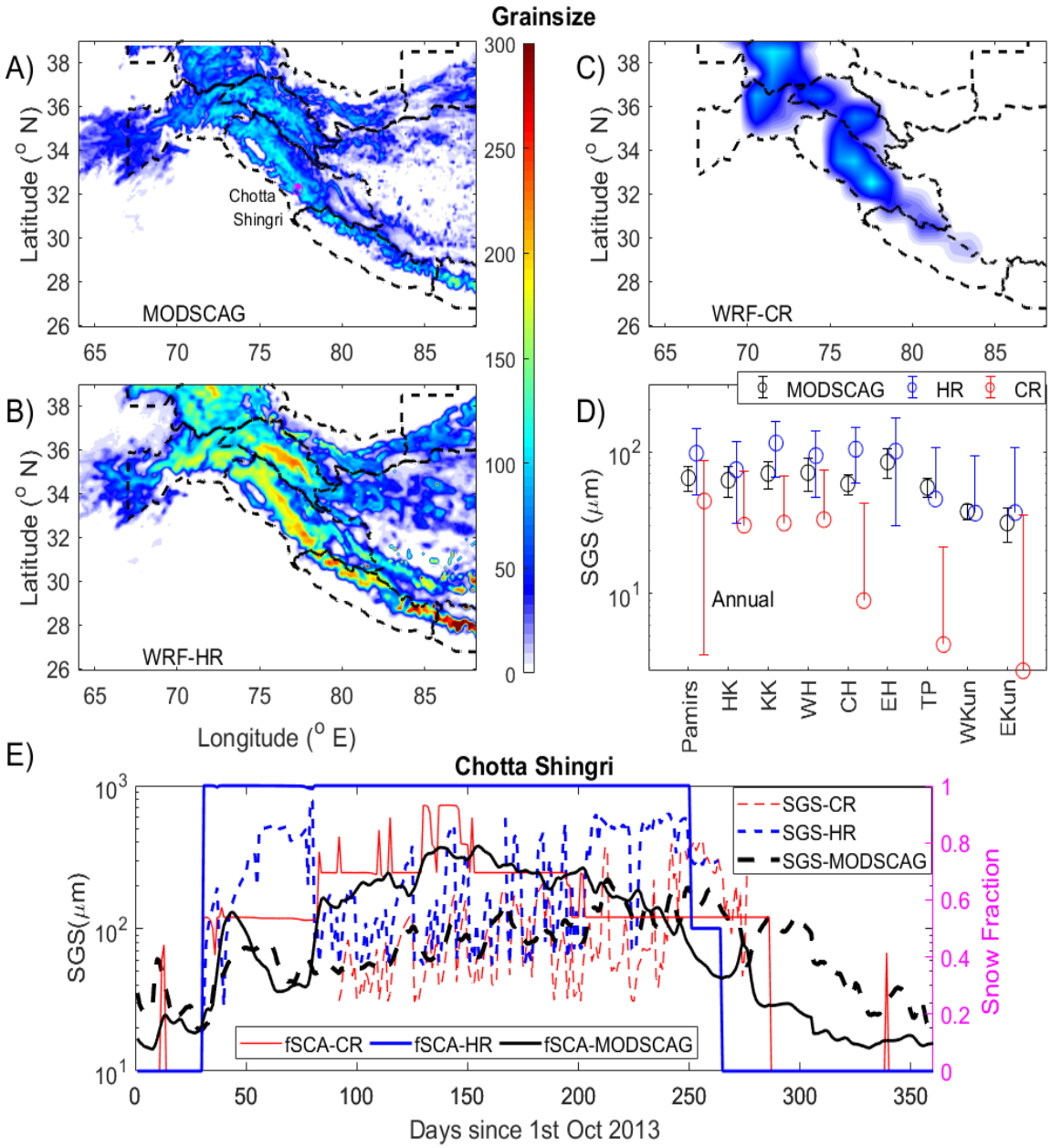

Figure 4: Spatial distribution of annual mean snow grain size (SGS) during midday (1000-1400 LT) for water year 2013-14 from A) STC-MODSCAG retrievals and simulated values from B) WRF-HR and C) WRF-CR runs is shown. Panel D illustrates the distribution of midday mean fSCA over each subregion identified by glacier classification following Randolph Glacier Inventory. The circle and vertical legs represent mean±standard deviation over each region for the entire year. Here, Hindu Kush, Karakoram, W.Himalayas, C.Himalayas, E.Himalayas, Tibetan Plateau, West Kunlun and East Kunlun regions are abbreviated as HK, KK, WH, CH, EH, TP, WKun and EKun, respectively. Panel E shows time-series of daily midday SGS (hashed lines) and fSCA (solid lines) from MODSCAG (black), WRF-HR (blue) and WRF-CR (red) over a grid located near the Chotta Shingri glacier (marked by magenta diamond in Figure 3A) of western Himalaya region.

Quite anomalous to other grids in HMA, the WRF-CR simulated SGS values over some grids near the Chotta Shingri glacier (marked by magenta circle in Figure 4A) of the western Himalaya sub-region are closer to STC-MODSCAG observations than that simulated by WRF-HR runs. As a sanity check, daily variation of SGS (hashed lines in Figure 4E) and fSCA (solid lines in Figure 4E) from STC-MODSCAG (black), WRF-HR (blue) and WRF-CR (red) over this glacier are compared. Fractional snow cover from STC-MODSCAG gradually increase from 0.2 in November, 2013 to 0.8 in February, 2014 and subsequently decrease back to 0.1 by September, 2014 at the glacier location. Corresponding SGS values from STC-MODSCAG closely followed the seasonal trend in fSCA varying around the values of 80-200 micron in winter. In comparison, simulated fSCA from WRF-HR values drastically increased to 1 at the beginning of November, 2013 (from no snow cover before that), remained fully snow covered till mid-June, 2014 and then suddenly became snow free after June. Compared to satellite estimates, fSCA from WRF-HR are greater in magnitude throughout the duration of snow cover indicating more snow mass simulated by WRF-HR. Associated SGS values (80-800 micron) simulated by WRF-HR are also greater than STC-MODSCAG estimates throughout the snow duration over the grid. However, the fSCA variation from WRF-CR over this grid is very close to the variation seen by STC-MODSCAG, and the associated SGS values (50-400 micron) from WRF-CR are also closer to the estimated STC-MODSCAG values, supporting our argument that biases in simulation of fSCA also affect the simulated annual mean SGS values.

The annual mean snow albedo (α) values and the distribution over each sub region from satellite estimates (by combing grain sizes from STC-MODSCAG and decrease in albedo from STC-MODDRFS (see Bair et al, 2016)) and simulated by both models are presented in Figure 5.

Highest annual mean α values (~ 0.65-0.75) are observed over mountain peaks in Karakoram, Pamirs and W.Himalaya regions (Figure 5A). The location and magnitude of annual mean α over these grids are closely reproduced in WRF-HR with an underestimation of < 10% (Figure 5B). WRF-CR simulated annual mean α values over these grids have a considerably larger underestimate of ~50% (Figure 5C). Similar statistics are prevalent over all the sub regions of HMA (Figure 5D). Specifically, the distribution of α values from WRF-HR nearly matches the observed distribution, but, the distribution of albedos from the coarser model, WRF-CR, are generally 0.2-0.3 lower when compared to the observations. The improvement of α estimation in WRF-HR runs compared to WRF-CR runs can be attributed to the relatively better simulation of fSCA (Figure 2), NSD (Figure 3) and SGS (Figure 4) in WRF-HR. Simulated annual mean α values are primarily the composite albedo values of snow covered grids. In WRF-Chem-SNICAR simulations, the composite albedo of a snow-covered grid box is computed as weighted average of representative area fractions of sub-grid snow-cover and snow-free regions. Thus, relatively lower values of simulated fSCA and NSD in WRF-CR runs compared to WRF-HR runs can contribute substantially to the relatively lower annual and seasonal mean α values simulated by WRF-CR. Note, the opposite nature in biases simulated by WRF-HR runs in mean albedo and SGS values. This is intuitive as smaller snow particles cover greater surface area and therefore reflect more solar radiation from the surface. A similar pattern in distribution of snow albedo from WRF-HR and WRF-CR are also found over the sub regions for pre-monsoon and winter months, separately (Figures 5E and 5F), indicating robust improvement in WRF-HR simulated albedo values throughout the year. The differences in simulated α in WRF-HR with the observations increased during pre-monsoon and were lower during winter. Here, it is worth

mentioning that we are comparing instantaneous estimates obtained from Terra overpass during 1000 LT with midday (1000-1400 LT) mean model values. The inherent diurnally in α values under clear sky conditions in pre-monsoon season (Bair et al., 2017) might contribute partially to the observed enhancement in differences during pre-monsoon season. At the same time, the mean α values from STC-MODSCAG (representative of only snow covered regions) are biases towards higher values than the corresponding simulated α values (composite albedo of the pixel) predominantly over the snow grids with annual mean fSCA are much smaller than 1.

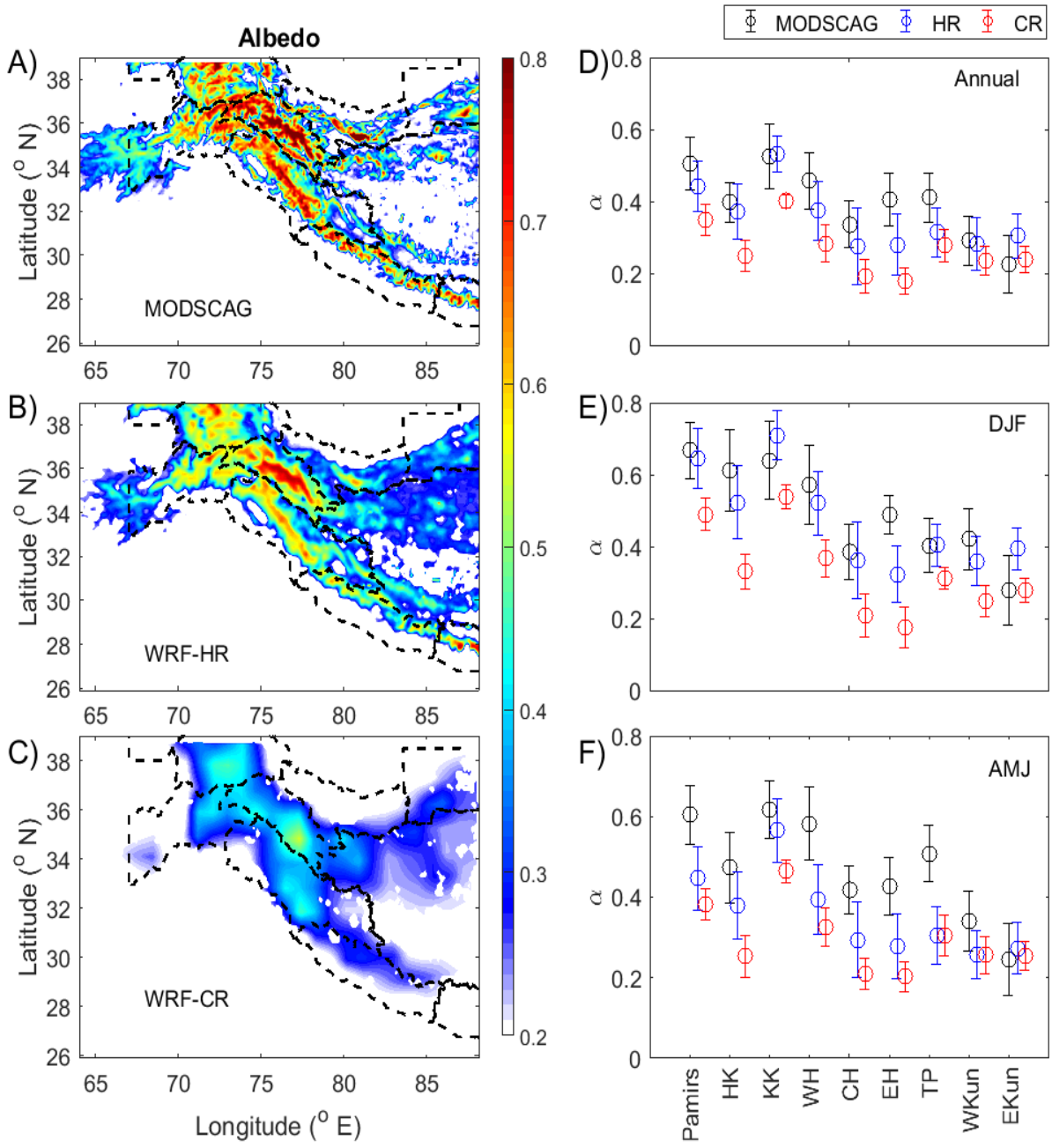

Figure 5: Spatial distribution of annual mean snow albedo (α) during midday (1000-1400 LT) for water year 2013-14 from A) STC-MODSCAG retrievals and simulated values from B) WRF-HR and C) WRF-CR runs is shown. Panels D-F illustrate the distribution of midday mean fSCA over each subregion identified by glacier classification following Randolph Glacier Inventory. The circle and vertical legs represent mean±standard deviation over each region for D) entire year, E) winter (December - February) and F) pre-monsoon (April - June) season, separately. Here, Hindu Kush, Karakoram, W.Himalayas, C.Himalayas, E.Himalayas, Tibetan Plateau, West Kunlun and East Kunlun regions are abbreviated as HK, KK, WH, CH, EH, TP, WKun and EKun, respectively.

3.2: Aerosol distribution and LAP in snow

We used available in-situ and ground sun photometer measurements from seven different sites across our study domain (location shown in Figure 6) to evaluate the simulated aerosol optical depth (AOD). The annual mean midday AOD at each site is shown in Figure 6A. Three sites (i.e. Merak, CAS and Kathmandu shown in Figures 6B-D) are located on the Himalaya slopes and the other four sites (Lahore, Jaipur, Kanpur and Gandhi College shown in Figures 6E-H) are located in the Indo-Gangetic Plains. In-situ measurements clearly illustrate a sharp decrease (4-5 fold) in mean AOD as we traverse higher up the Himalayan slope. The annual mean AOD for Lahore and Kanpur sites are 0.41 and 0.52, respectively, while the AOD over high elevated sites i.e. Merak and CAS sites are 0.07 and 0.05, respectively. Also, MODIS-observed AOD values prominently show the reduction in annual mean AOD from the Indo-Gangetic Plains (MODIS-AOD ~ 0.4-0.7) to the Tibet region (MODIS-AOD ~ 0.1-0.2) (Figure S5). Over the four sites in the Indo-Gangetic Plains, AOD simulated by both WRF-HR and WRF-CR runs are well correlated with observations (r= 0.5-0.6, Figures 6E-6H). The biases in modelled AOD are also similar (in the range of 0.2-0.4) in case of both WRF-HR and WRF-CR runs (Figures 6E-6H). Thus, no significant improvement in AOD values are achieved over the plain region with fine resolution. However, distinct and large improvement in simulated AOD is seen over the high elevation sites due to the increase in spatial resolution. Note that AOD values from WRF-CR are not strongly correlated with observations at these sites (Figures 6B-6D) and also have very high positive biases in AOD values (even higher than annual mean values at Merak and CAS stations). In contrast, the correlation between observations and WRF-HR is reasonably good (r=0.5-0.8 at these sites) using fine spatial resolution in WRF-HR. The positive biases in AOD from WRF-HR at Merak and

CAS sites are lower than corresponding WRF-CR values by an order of magnitude. Presence of lower biases in AOD from WRF-HR over high elevation sites indicates that the observed sharp decrease in AOD values across the Himalayan slope are better captured by the higher resolution WRF run (WRF-HR) than in the coarser run. Greater annual mean AOD value is simulated by WRF-CR over the entire HMA region compared to WRF-HR (Figure S5) supporting an overestimation of AOD from WRF-CR at higher elevation in addition to the few sites. The presence of high biases (0.3-0.4) over Kathmandu valley even in WRF-HR runs indicate that model resolution even finer than 12 km is likely needed to better resolve the AOD distribution in complex terrain around valleys in Himalayan slope regions. Moreover, Jayarathne et al., 2018 shows that many local emissions are not accounted in coarse emissions which causes underestimation in simulated regional AOD values in these valleys. Temporal variability in monthly mean AOD (relatively higher AOD in pre-monsoon) is simulated reasonably well by both the model versions (Figure S5).

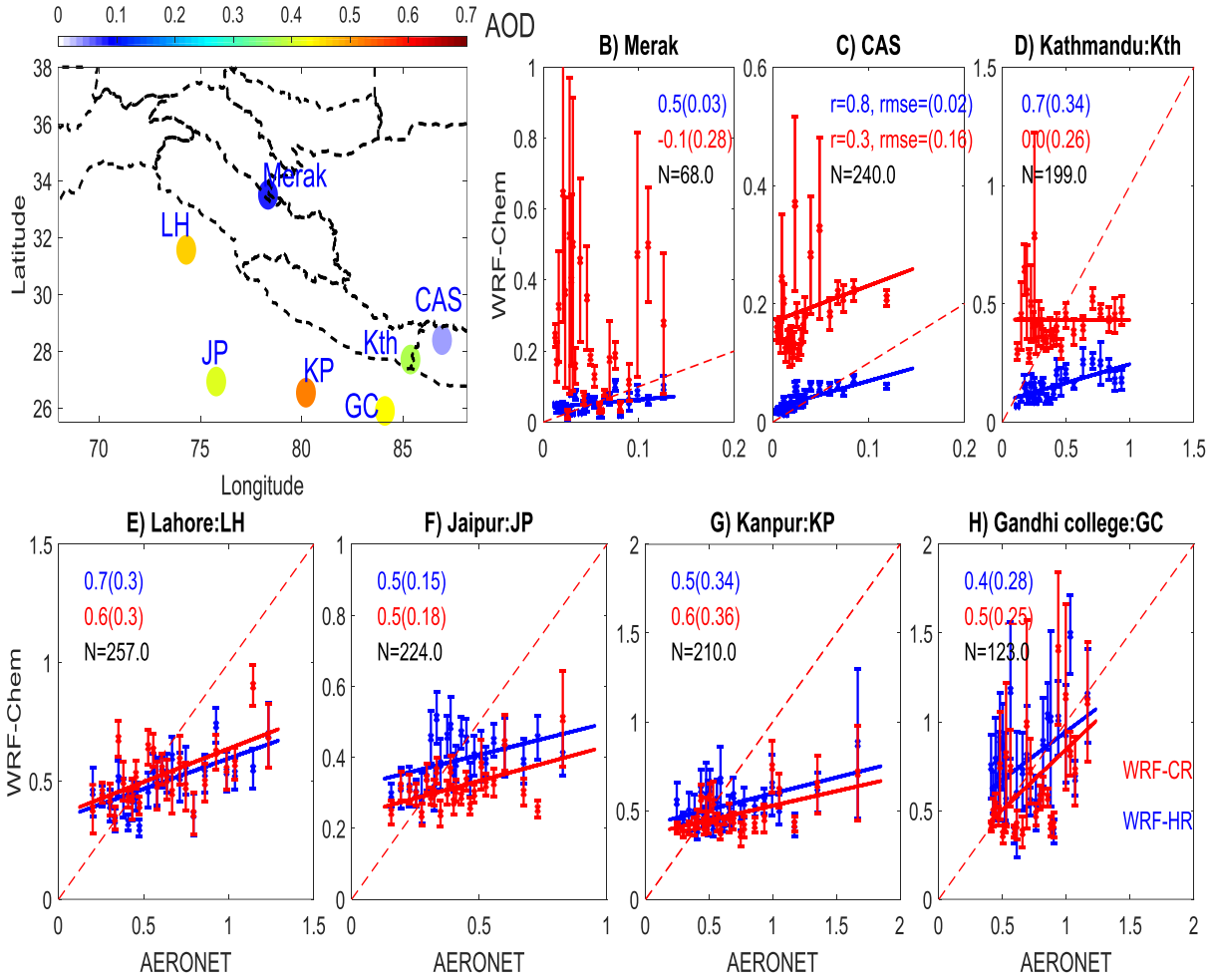

Figure 6: Comparison of midday (averaged over 1000-1400 LT) aerosol optical depth (AOD) measured by ground based sun photometer at seven sites within the study domain with corresponding simulated AOD values from, both, WRF-HR and WRF-CR. The annual mean AOD values over each site is shown by shade in topmost left Panel. The other panels illustrates the comparison over one of each stations shown by dots in topmost left Panel. The 'N' mentioned in the legend in each panel is the total number of days when collocated data between model and measurement is available over that site. These sample points are divided into 50 equal bins of ascending AERONET-AOD values (2 percentile each) and averaged. The standard deviation in each bin is shown by the vertical bars. The correlation coefficient values (r) are also mentioned in the legend followed in brackets by the relative error values (∑rmse/mean obs).

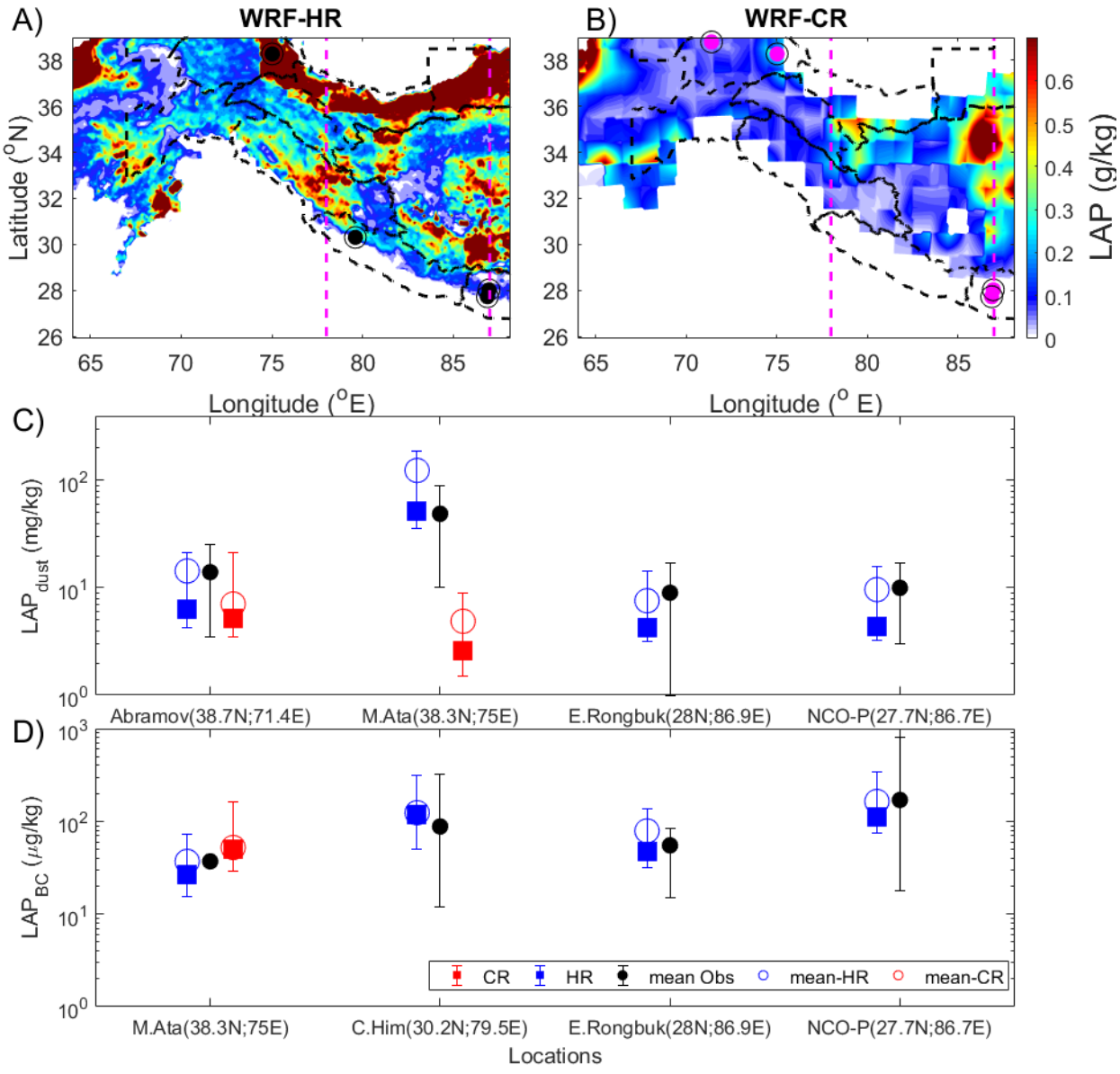

Figure 7: Spatial distribution of annual mean LAP concentration in snow top layer for water year 2013-14 simulated by A) WRF-HR and B) WRF-CR. The black dots in Panel A denote the locations where observations of BC in snow is available. Similarly, the magenta dots in Panel B

denote the locations from where observation of dust in snow is available. Panels C-D illustrate comparison of simulated LAP_{BC} (top) and LAP_{dust} (bottom),respectively, in topmost snow layer with observed values over the marked locations in the Himalayan cryosphere. Simulated annual mean (circle) and distribution of midday mean LAP values (box plot) is shown. The top (bottom) edge of the box plot represent 75 (25) percentile of the distribution. The WRF-HR and WRF-CR values are represented by blue and red, respectively. The pink lines in Panel A are the cross-sections shown in Figure 8.

Significant differences in simulated AOD over high elevations of Himalaya slopes and TP indicate that considerable differences might also be present in LAP concentrations in snow between the two WRF simulations. Annual mean LAP concentrations in top snow layer from WRF-HR and WRF-CR simulations are compared in Figures 7A-7B. The comparison shows that LAP concentration in WRF-HR are significantly higher than WRF-CR simulated values. Quantitatively, the WRF-HR simulated annual mean LAP concentrations over the Pamir (0.5 g/kg), Karakoram (0.45 g/kg), Hindu Kush (0.2 g/kg), W. Himalaya (0.3 g/kg), C. Himalaya (0.2 g/kg) and E. Himalaya (0.08 g/kg) ranges is 3-5 times higher than the same from WRF-CR runs. In contrast, WRF-HR simulated LAP over TP (0.21 g/kg) and Kunlun ranges (0.8 g/kg) is similar to the mean magnitude simulated by WRF-CR runs. As a sanity check, we evaluate the simulated LAP concentrations against those previously reported in the literature. Figures 7C and 7D illustrate the evaluation of mean annual LAP concentration from WRF-HR and WRF-CR associated with BC (LAP_{BC}) and dust (LAP_{dust}), respectively, against the reported data (shown as filled black circles). The locations of reported LAP_{BC} (black filled dots) and LAP_{dust} (magenta filled dots) are shown in Figure 7C and Figure 7D, respectively. First, the difference in the magnitude of LAP_{dust} and LAP_{BC} over HMA is striking. The LAP_{dust} is more than 1000 times greater than LAP_{BC} both in observations and the models. Secondly, LAP_{BC} and LAP_{dust} values from WRF-HR are much closer to reported values compared to WRF-CR values. The differences in mean of

reported LAP_{BC} and LAP_{dust} distribution to that simulated by WRF-HR at various sites are in range of 5-30 µg/kg and 5-20 mg/kg, respectively. WRF-CR well simulates the concentrations of LAP_{BC} and LAP_{dust} over Pamirs (~ 10 mg/kg), but significantly underestimates the LAP_{BC} and LAP_{dust} (by an order of magnitude) over the Himalayan ranges. Thus, the WRF-HR better simulates aerosol and LAP concentration than the WRF-CR over the HMA region.

It is interesting to note that finer spatial resolution resulted in lower AOD but greater LAP values in snow over some places in HMA. For more insight, the vertical distribution of aerosol concentration in altitude-latitude space (Figure 8) across two latitudinal cross-sections (magenta colored lines in Figure 7A) is analyzed. Figure 8 illustrates the differences in simulated vertical distribution of mean aerosol number concentration along 78^{o}E (row 1) and 87^{o}E (row 2) for WRF-HR (left column) and WRF-CR (right column) runs, respectively. Corresponding terrain elevation (black solid line) and snow depth (magenta bars) are also overlaid in these plots. The latitude-altitude plots clearly illustrate that improved representation of the terrain in WRF-HR shows the sharp change of elevation over Himalayan foothills and causes a steeper natural barrier to the transport of aerosols uphill from IGP to HMA region than in the WFR-CR model. Also, high spatial resolution enhances snowfall in WRF-HR over the HMA region relative to the WRF-CR model. While the former change increased annual dry deposition flux, more snowfall caused greater wet deposition annually in WRF-HR compared to WRF-CR (Figure S6). The combination of these effects increases the deposition of aerosols and therefore LAP on the southern slopes of Himalaya in the WRF-HR run. This explains the coexistence of higher LAP concentration/deposition and lower AOD across HMA in WRF-HR, compared to corresponding WRF-CR results.

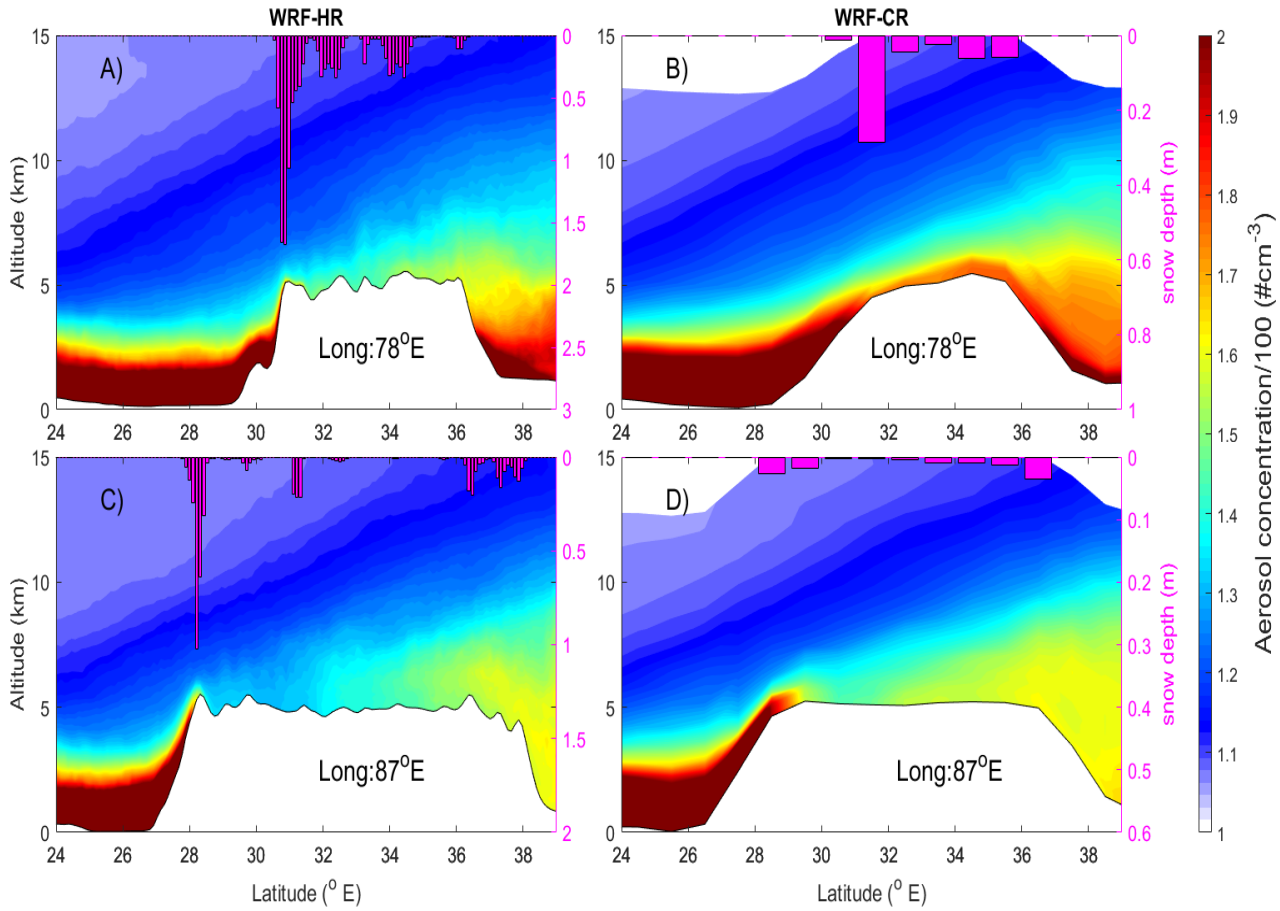

Figure 8: Longitudinally-averaged annual mean aerosol number concentration plotted in altitude-latitude space for two longitudinal traverses across the study domain, i.e. 78°N (Panels A and B) and 87°N (Panels C and D) for both WRF-HR (left column) and WRF-CR (right column). Corresponding terrain elevation is shown in solid black line. Corresponding to each latitude, the longitudinally-averaged annual mean snow depth is also presented in magenta color bars (using y-axis on the right).

3.3 LAP-induced Snow darkening and radiative forcing

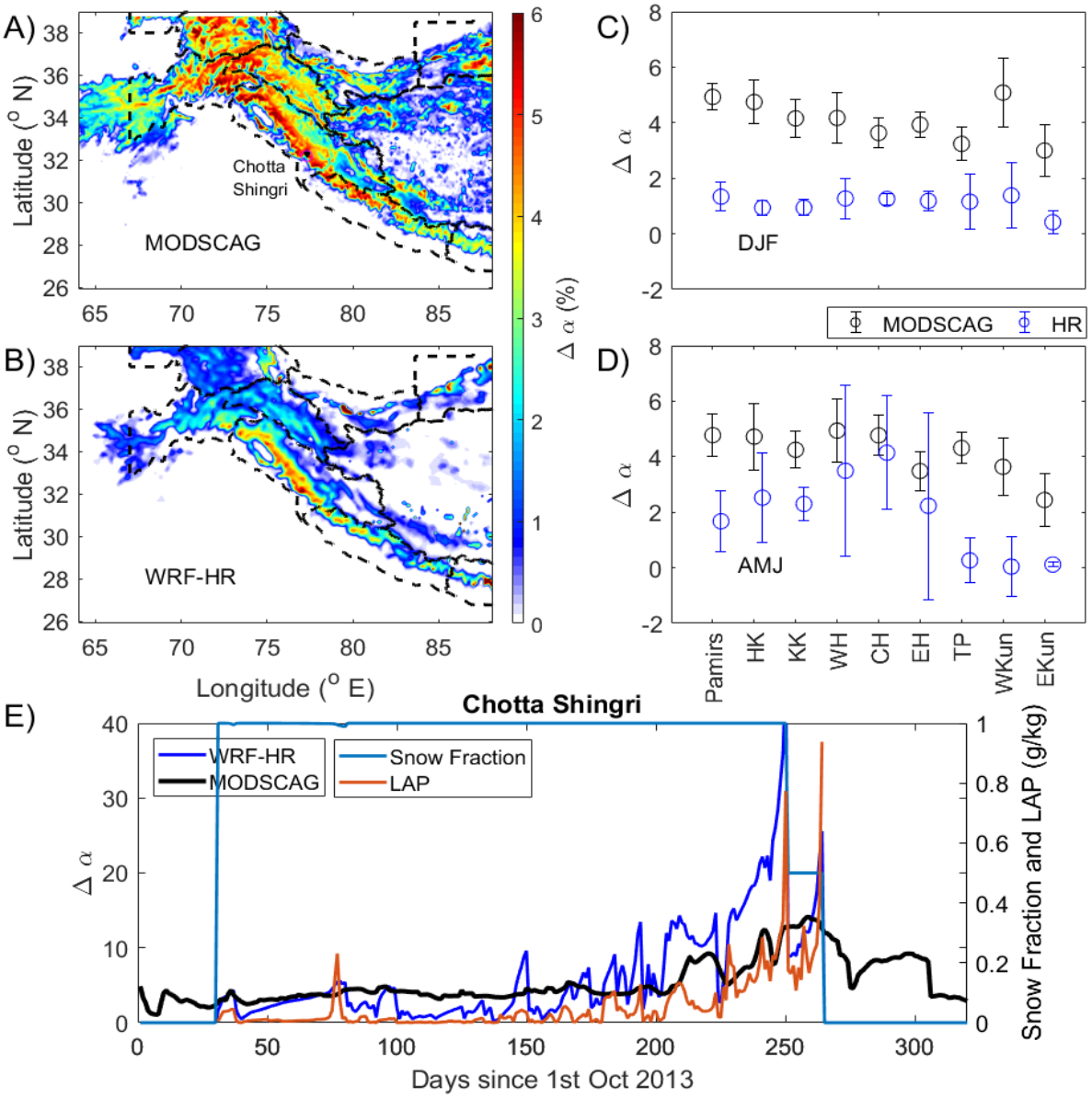

Figure 9: Spatial distribution of annual mean LAP-induced snow albedo darkening (Δα) during midday (1000-1400 LT) for water year 2013-14 from A) MODSCAG retrievals and B) simulated values from WRF-HR is shown. Panels C and D illustrate the distribution of midday mean Δα over each sub region identified by glacier classification following Randolph Glacier Inventory. The circle and vertical legs represent mean±standard deviation over each region for entire year. Here, Hindu Kush, Karakoram, W.Himalayas, C.Himalayas, E.Himalayas, Tibetan Plateau, West Kunlun and East Kunlun regions are abbreviated as HK, KK, WH, CH, EH, TP, WKun and EKun, respectively. Panel E shows time-series of daily midday Δα from STC-MODSCAG (black) and WRF-HR (blue) over the grids located near the Chotta Shingri glacier (marked in Figure A) of western Himalaya region. Also fractional snow cover and LAP concentrations from WRF-HR over the same grids are included.

STC-MODDRFS retrievals illustrate that locations in Hindu Kush and W. Himalayas have the highest annual mean LAP-induced reduction in snow albedo (Δα in %) followed by Karakoram, C.Himalayas and Pamir regions (Figure 9A). WRF-HR simulated the spatial variations in annual mean Δα reasonably well (Figure 9B), but, the magnitudes are underestimated by ~20-40 % throughout the domain. Note that the biases in annual mean values are lowest over grids in Himalayan ranges (where the underestimation is within 20%). Season wise and region wise distribution plots show that the WRF-HR biases are higher in winter months than the pre-monsoon months (Figures 9C and 9D). While, WRF-HR simulated Δα values in the winter span between 1-3 %, the corresponding STC-MODDRFS estimates of Δα are larger with values ranging between 3-6% (thus no overlap with model values) over all the sub regions. In pre-monsoon months, the distribution of modeled WRF-HR Δα values over Karakoram and Himalayan ranges are similar in magnitude, explaining the lower biases in annual mean values over Himalayas. This spatiotemporal variability in differences between STC-MODDRFS retrievals and simulated Δα values is consistent with the variability in biases of fractional snow cover seen in WRF-HR (Figures2E and 2F). For a closer look, the difference in daily midday mean Δα values from STC-MODDRFS (black) and WRF-HR (blue) are compared (in Figure 9E) over the grids of Chotta Shingri glacier (similar as Figure 4E). Corresponding, midday mean fSCA (light blue) and LAP (orange) from WRF-HR are also plotted. Δα values from STC-MODDRFS are about 5% during winter months, but, increases in pre-monsoon months until mid-June (peak value is 18%). Albedo reduction is closely associated with the temporal progression in midday LAP concentration in snow over this region at daily scale. In agreement, midday Δα values from WRF-HR are lower in winter months and higher in pre-monsoon

months. Except occasional peaks, with magnitudes of 3-4 %, Δα values from WRF-HR largely remained below 3 % till late February. A steep increase in Δα values from WRF-HR is seen in March (monthly mean ~ 4%), April (9%), May (13%) and June (18%).

As already discussed, the simulated fSCA values in WRF-HR are greater than observed fSCA from STC-MODSCAG for most of the winter season (Figure 4E). Specifically, the underestimation in WRF-HR simulated Δα values (Figures 9C and 9D) in winter over Karakoram, Hindu Kush and Himalayas is in agreement with corresponding overestimation of WRF-HR simulated fSCA values over these regions (Figure 2). STC-MODDRFS estimated Δα is based on surface reflectance, while Δα calculated by model involves the surface layer depth. The surface snow layer in SNICAR/CLM continuously evolves as fresh snowfall is added or with snow melting, so the LAP concentrations in the surface layer depend on new snowfall, meltwater flushing, and layer combination/division (Flanner et al., 2007; Flanner et al., 2012; Oleson et al., 2010). Therefore, more precipitation and more snow coverage in winter can be a primary factor causing the underestimation of annual mean LAP concentration and LAP-induced snow darkening. Secondly, the associated overestimation in simulated SGS during winter (Figure 4) can also contribute to the lower Δα values simulated in WRF-HR because bigger snow grains in WRF-HR lead to lower clean albedo and thus smaller percentage reduction in albedo compared to STC-MODDRFS. Moreover, we have assumed spherical shaped snow grains in our simulations. Recently, microscopic level studies show that uncertainties associated with simplified snow grain shape treatment in model parameterization can solely contribute to large biases in SNICAR-Δα estimates and thus the LAP-snow albedo radiative and snow melt feedback processes (Liou et al., 2014; Dang et al., 2016; He et al., 2017). Thirdly, the fact that the

persistent cloud cover over HMA during winter season can induces a lot of uncertainty in the STC-MODSCAG and STC-MODDRFS estimates, is also equally important.

At the same time, uncertainties regarding aerosol emission, transport and deposition to the snow layers are also significant. It is well known that the transport and deposition of black carbon from Indian landmass to Himalayas increases in the afternoon with the evolution of boundary layer over the IGP region (Dumka et al., 2015;Raatikainen et al., 2014). This feature is well simulated by the model (not shown). As STC-MODDRFS estimates are representative of 1000 LT, but simulated values are sampled in the midday (1000-1400 LT), positive biases in aerosol transport and deposition in snow packs (i.e. higher Δα values) might be simulated in WRF-HR runs, especially during pre-monsoon months. At the same time, GOCART dust emission parameterization (used here) is dependent on near surface wind speed. Previous studies have evaluated and illustrated inherent uncertainties in dust emission by this parameterization, mostly underestimation over Indian region (Dipu et al., 2013; Kumar et al., 2014). Thus, the uncertainty in local dust emission fluxes over HMA can also contribute to the biases in simulated Δα values. Also, large biases in LAP values may be simulated due to model uncertainties in enhanced wet scavenging fluxes in winter. An overestimation in LAP concentration can lead to an overestimation of snow darkening and melting, resulting in an underestimation of NSD (Figure S4). The large biases in Δα values (> 20 %) simulated by WRF-HR towards late spring could be attributed to both, underestimation in fSCA and overestimation of LAP concentration in the model.

Although a better quantification of these model biases requires evaluation against in-situ measurements, it is worth mentioning here that no in-situ measurements are available for

a direct comparison of these high Δα values WRF-HR over W. Himalayas (Gertler et al., 2016). Nonetheless, the high values simulated during pre-monsoon are close to previously reported values over other HMA regions. Kaspari et al., (2014) used the offline SNICAR model to report that BC concentrations in pre-monsoon snow/ice samples at Mera Glacier were large enough to reduce albedo by 6-10% and the reduction in albedo was 40-42% relative to clean snow when dust is included in the calculation. Recently, Zhang et al. (2018) has combined a large dataset of LAP measurements in surface snow with the offline SNICAR model to illustrate that Δα can be >35% over Tibetan Plateau. Moreover, the composite effect of this discrepancy on seasonal/annual mean values is minimal as the snowpack is at its minimum near the end of pre-monsoon season. Similar high daily variability, huge radiative forcing values (LAPRF ~200 W/m2) and sudden decline in snow depth in late pre-monsoon is also reported over upper Colorado river basin (Skiles et al., 2015; Skiles and Painter, 2017)

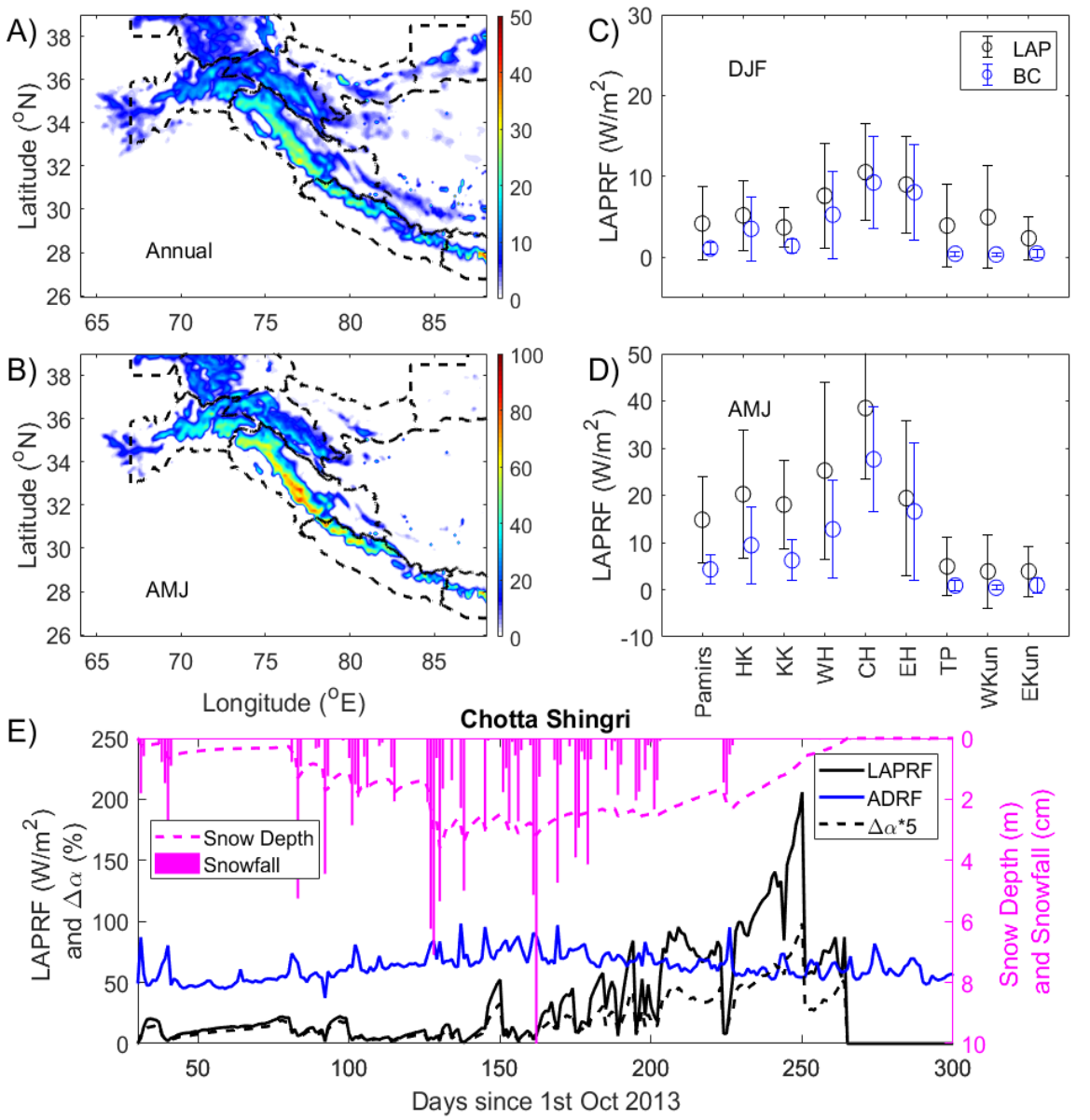

Figure 10: A) Spatial distribution of annual mean snow mediated LAP-induced radiative forcing (LAPRF) from WRF-HR and B) Spatial distribution of seasonal mean LAPRF over snow covered for pre-monsoon season (AMJ) of water year 2013-14. Panels C and D illustrate the distribution of LAPRF (blue) and BC-only-LAPRF (black) over each sub region identified by glacier classification following Randolph Glacier Inventory for winter and pre-monsoon, respectively. The circle and vertical legs represent mean±standard deviation over each region for entire year. Here, Hindu Kush, Karakoram, W.Himalayas, C.Himalayas, E.Himalayas, Tibetan Plateau, West Kunlun and East Kunlun regions are abbreviated as HK, KK, WH, CH, EH, TP, W.Kun and E.Kun, respectively. Panel E shows time-series of daily midday LAPRF (blue) and aerosol direct radiative forcing at surface (ADRF, blue) over the Chotta Shingri region (marked in Figure 9A) of western Himalaya region. The simulated LAP-induced change in snow albedo is also shown in hashed black line. Also snow depth and snowfall from WRF-HR over the same grid is included.

In agreement with the spatial variation in Δα values, the annual mean snow-mediated LAP-induced radiative forcing (LAPRF) from WRF-HR over grids in W.Himalayas and C. Himalayas are highest followed by Karakoram, Hindu Kush, E.Himalayas and Pamir regions (Figure 10A). The spatial distribution of pre-monsoon mean LAPRF values from WRF-HR (Figure 10B) is similar to that of the annual mean LAPRF values, but, the pre-monsoon magnitudes are higher by an order of magnitude throughout most of the domain. This is mainly due to the large increase in Δα values in pre-monsoon when LAPs aggregate on the surface compared with winter months when LAPs are continuously covered by new snow (Figure 9). Spatio-temporal variability in LAPRF is evident in the seasonal and regional distribution plots (Figure 10C and 10D). LAPRF values over the edges of HMA are greater than the highland TP region in both winter and pre-monsoon months probably due to greater LAP deposition simulated over Hindu Kush, Karakoram and Himalayas regions (Figure S7) from the close proximity of dust sources. Also, it is clearly visible that the maximum LAPRF values within HMA region are present over grids in Himalayan ranges (during both winter and pre-monsoon) with annual mean values > 50 W/m^2 (seen in Figures10B and 10D) and maximum instantaneous values higher than 150 W/m^2 (not shown). The time series of midday mean LAPRF values (Figure 10E) over the same grids in the Chotta Shingri Glacier region in western Himalaya is plotted to ascertain possible daily variability in LAPRF for midday over the region. Corresponding LAP-induced albedo reduction, snow depth and snowfall values are also plotted to show how LAPRF can affect local snow melting. The daily snow depth increases to 3.6 m in winter (30-150 days) followed by gradual reduction and snow cover melting in pre-monsoon (150-270 days). The mean midday LAPRF value is ~10 W/m^2 in winter season, but, the magnitude increased gradually during March (18

W/m^2), April (44 W/m^2), May (86 W/m^2) and June (123.5 W/m^2), eventually terminating with a peak value of 202 W/m^2 in mid-June. The temporal evolution in Δα values closely followed the LAPRF values with a variation in range of 1-20%. The shortwave aerosol direct radiative forcing (ADRF) during midday at the surface over the same grid is also shown (as blue curve) in Figure10E. The momentarily high values of ADRF during the period indicate dust storms or sudden increase in aerosol loading over the grid. A closer look illustrate that the large daily variations in LAPRF and Δα are associated with the variability in ADRF and daily snowfall occurence over the grid. Fresh snowfall feedbacks result in subsequent reduction in LAPRF and enhancement in snow depth (Figure10E), while, higher aerosol loading over aged snow is followed by a clear increase in LAPRF. During melting, our model considers that only a fraction of LAP is washed away with meltwater, which, results in enhanced concentration of LAP during the end stages of the snowpack. This snow albedo feedback along with the momentary high aerosol loading (on 250^{th} day) can explain the very high values of albedo reduction and LAPRF that were simulated during the last days of the snow cover over this grid. Higher LAPRF values indicate more energy being absorbed by the snow pack and thus more snow melting. Therefore, LAP-induced snow melting effect over Himalaya is very significant and is the largest relative to other areas within HMA.

Snow-mediated radiative forcing only due to BC- deposition is shown in Figures10C and 10D. Although, similar spatiotemporal pattern in LAPRF and BC-only-LAPRF is simulated, contrasting features in context to BC contribution to LAPRF are present in between the western part and eastern parts of HMA. During winter, the magnitude of BC-only LAPRF values is similar to that of total LAPRF over the western part of HMA region (i.e. Pamirs, Karakoram, Hindu Kush

and W.Himalayas) suggesting that BC is a dominant contributor to net LAPRF (Figures10C). But, large differences between LAPRF and BC-only LAPRF is present during pre-monsoon season over the western regions indicating that dust contribution is more or less equal to that of BC contribution over these regions (Figure10D). In contrast, the dust contribution to LAPRF values over the eastern domain (TP and Kunlun regions) is significant during winter season (Figures10C and 10D). The spatiotemporal variability in dust and BC contribution is reported previously and is mainly linked with the seasonal variability in meteorology and associated advection of South Asian emissions (Zhang et al., 2015; Wang et al., 2015a ; Niu et al., 2018). The ADRF-induced surface cooling effect may nullify the effects of LAPRF-induced warming effect on snowpack melting. But, the drastic increase in LAPRF values in April through June causes the magnitude of LAPRF to be twice that of ADRF over W. Himalayas during snow melting period, highlighting dominance of LAPRF (as also seen in Figure10E).

The simulated annual mean, pre-monsoon mean and BC-only-LAPRF values from WRF-HR are in general, higher compared to previously reported estimates of LAPRF from model studies at coarser resolution. For example, Ménégoz et al., (2014) have reported annual mean LAPRF of ~ 1-3 W/m^2 over Himalaya using an online simulation at 50 km resolution grid. Similarly, Qian et al., (2011) used the Community Atmosphere Model version 3.1 at coarser spatial resolution to show that simulated aerosol-induced snow albedo perturbations can generate LAPRF values of 5-25 W/m^2 during pre-monsoon over HMA. Also, coarsely resolved GEOS-Chem runs simulated BC-only-LAPRF can vary from 5 to 15 W/m^2 in the snow-covered regions over the TP (Kopacz et al., 2011). Recently, a decade long simulation using the RegCM model at 50 km spatial resolution also estimated maximum BC-only-LAPRF values of 5-6 W/m^2

over the Himalaya and southeastern TP averaged over non-monsoon season (Ji, 2016). However, the comparison of WRF-HR and WRF-CR simulations provided in this study clearly show that the magnitudes of snow macro- and micro-properties, aerosol loading and LAP-induced albedo darkening over Himalayas improved significantly with finer spatial resolution. Thus, the global model simulated LAPRF values are likely underestimated. In agreement, recently, Zhang et al., (2018) has estimated BC-only-LAPRF of 20-35 W/m^2 using offline SNICAR calculation forced with a greater coverage of measurements of surface snow content. He et al., (2018) have also reported similar high BC-only-LAPRF values after implementing a realistic snow grainsize parameterizations in offline SNICAR calculations over HMA.

4. Summary and Implications

In this study, we use the SNICAR model coupled with WRF-Chem regional model at high spatial resolution (WRF-HR; 12 km) to simulate the transport, deposition, and radiative forcing of light absorbing particles (LAPs; mainly Black Carbon and dust) over the high mountains of Asia (HMA) during water year 2013-14. The snow grain sizes and LAP-induced snow darkening was evaluated, for the first time, against comprehensive satellite retrievals (the MODSCAG and MODDRFS spatial and temporally complete retrieved satellite observations) over HMA. The atmospheric aerosol loading is evaluated against satellite and ground-based AOD measurements over HMA region. Results from another simulation which employ the same model configuration but a coarser spatial resolution (WRF-CR; 1 degree) are also compared

with WRF-HR to illustrate the significance of a better representation of terrain on snow-pack and aerosol simulation over HMA. The main conclusions from our study are:

a) The simulated macro- and micro-physical properties and the duration of snow packs over HMA improve significantly due to the use of fine spatial resolution, especially over the southern slopes of Hindu Kush and Himalayan ranges.
b) Simulated aerosol loading over HMA is also more realistic in WRF-HR than in WRF-CR, which leads to a reduction in biases of annual mean LAP concentration in snow. This improvement is attributed to a more realistic simulation of wet deposition (due to a better simulation of snow pack) and dry deposition of LAPs (associated with a better representation of terrain) in WRF-HR.
c) WRF-HR captures the magnitude of LAP-induced snow albedo reduction ($\Delta\alpha$) over Himalayas and Hindu Kush region relatively well compared to the STC-MODDRFS retrievals during pre-monsoon. However, during winter, large biases in modelled $\Delta\alpha$ values are present. This is probably due to inherent uncertainties in model parameterizations and satellite retrievals associated with the cloud cover over HMA in winter period.
d) The glaciers and snow cover regions located in the Himalaya have the highest LAPRF within HMA i.e. annual mean LAPRF ~ 20 W/m^2 and pre-monsoon mean LAPRF ~ 40 W/m^2. This is consistent with similar high values of $\Delta\alpha$ over Himalayan ranges i.e. annual mean $\Delta\alpha$ values ~ 2-4 % and pre-monsoon mean $\Delta\alpha$ values ~ 4-8 %. The annual mean LAP concentration in snow values (200-300 mg/kg) are also high. Thus, the Himalaya (more specifically, western Himalayas) is most vulnerable to LAP-induced snow melting within HMA.

Ramanathan and G. Carmichael, (2008) suggest that atmospheric warming from LAPs (~20 W/m^2) may be just as important as greenhouse gases in the melting of snowpack and glaciers over Asia. In this context, the high magnitudes of LAPRF values in pre-monsoon over HMA (~ 40 W/m^2) clearly shows that snow-mediated aerosol forcing on snow melting over HMA can be twofold the significance of the atmospheric forcing. Nonetheless, the differences in snow surface properties between WRF-HR and satellite observations indicate probable uncertainties in model parameterizations. At the same time, the STC-MODDRFS retrievals themselves may have an uncertainty of ~ 5% in instantaneous $\Delta\alpha$ measurements. Thus, efforts to further reducing the LAPRF uncertainties in the model are warranted in the future by using in-situ observations (i.e. field campaigns), specifically over the most affected western Himalayas, where relevant measurements are largely absent (Gertler et al., 2016). Moreover, satellite retrievals will be markedly improved in the coming decade with the NASA Decadal Survey Surface Biology and Geology imaging spectrometer mission, which includes as a core measurement snow albedo and its controls (National Academies of Science, 2018). These visible through shortwave infrared imaging spectrometer retrievals have uncertainties an order of magnitude smaller (Painter et al., 2013) than those from multispectral sensors such as MODIS and will provide a more accurate constraint on the physically-based modeling pursued here.

Author contribution:

CS did the modeling, analysis and wrote the paper under the supervision of YQ. KR, KB and TP created the STC-MODSCAG and STC-MODDRFS datasets. All authors provided advice and feedback throughout the analysis, drafting and submission process.

Acknowledgment

This research was supported by the NASA High Mountain Asia Project. The Pacific Northwest National Laboratory (PNNL) is operated for DOE by Battelle Memorial Institute under contract DE-AC06-76RLO 1830. Part of this work was performed at the Jet Propulsion Laboratory, California Institute of Technology under contract with NASA. H. Wang acknowledges support from the U.S. Department of Energy (DOE), Office of Science, Biological and Environmental Research as part of the Earth System Modeling program. We thank the PIs of the selected AERONET and SKYNET stations, for providing the data used in this study. The AERONET data are obtained from the AERONET website, http://aeronet.gsfc.nasa.gov/. We also thank the PI of the selected SkyNet station, for providing the data used in this study. The SkyNet data is obtained from the website http://atmos3.cr.chiba-u.jp/skynet/merak/merak.html/.

References

Amante, C. and Eakins, B. W.: ETOPO1 1 Arc-Minute Global Relief Model: Procedures, Data Sources and Analysis., 2009.

Azam, M. F., Ramanathan, A., Wagnon, P., Vincent, C., Linda, A., Berthier, E., Sharma, P., Mandal, A., Angchuk, T., Singh, V. B. and Pottakkal, J. G.: Meteorological conditions, seasonal and annual mass balances of Chhota Shigri Glacier, western Himalaya, India, Ann. Glaciol., 57(71), 328–338, doi:10.3189/2016AoG71A570, 2016.

Bair, E. H., Rittger, K., Davis, R. E., Painter, T. H. and Dozier, J.: Validating reconstruction of snow water equivalent in California's Sierra Nevada using measurements from the NASA Airborne Snow Observatory, Water Resour. Res., 52(11), 8437–8460, doi:10.1002/2016WR018704, 2016.

Barnard, J. C., Fast, J. D., Paredes-Miranda, G., Arnott, W. P. and Laskin, A.: Technical note: Evaluation of the WRF-Chem "Aerosol chemical to aerosol optical properties" module using data from the MILAGRO campaign, Atmos. Chem. Phys., 10(15), 7325–7340, doi:10.5194/acp-10-7325-2010, 2010.

Barnett, T. P., Adam, J. C. and Lettenmaier, D. P.: Potential impacts of a warming climate on water availability in snow-dominated regions, Nature, 438(7066), 303–309, doi:10.1038/nature04141, 2005.

Binkowski, F. S. and Shankar, U.: The Regional Particulate Matter Model. 1. Model description

and preliminary results, J. Geophys. Res., 100(D12), 26191–26209, doi:10.1029/95JD02093, 1995.

Bolch, T., Kulkarni, A., Kääb, A., Huggel, C., Paul, F., Cogley, J. G., Frey, H., Kargel, J. S., Fujita, K., Scheel, M., Bajracharya, S. and Stoffel, M.: The state and fate of himalayan glaciers, Science (80-.)., 336(6079), 310–314, doi:10.1126/science.1215828, 2012.

Bollasina, M. A., Ming, Y. and Ramaswamy, V.: Anthropogenic Aerosols and the Weakening of the South Asian Summer Monsoon, Science (80-.)., 334(6055), 502–505, doi:10.1126/science.1204994, 2011.

Bonasoni, P., Laj, P., Marinoni, A., Sprenger, M., Angelini, F., Arduini, J., Bonafè, U., Calzolari, F., Colombo, T., Decesari, S., Di Biagio, C., Di Sarra, A. G., Evangelisti, F., Duchi, R., Facchini, M. C., Fuzzi, S., Gobbi, G. P., Maione, M., Panday, A., Roccato, F., Sellegri, K., Venzac, H., Verza, G. P., Villani, P., Vuillermoz, E. and Cristofanelli, P.: Atmospheric Brown Clouds in the Himalayas: First two years of continuous observations at the Nepal Climate Observatory-Pyramid (5079 m), Atmos. Chem. Phys., 10(15), 7515–7531, doi:10.5194/acp-10-7515-2010, 2010.

Bond, T. C., Doherty, S. J., Fahey, D. W., Forster, P. M., Berntsen, T., Deangelo, B. J., Flanner, M. G., Ghan, S., Kärcher, B., Koch, D., Kinne, S., Kondo, Y., Quinn, P. K., Sarofim, M. C., Schultz, M. G., Schulz, M., Venkataraman, C., Zhang, H., Zhang, S., Bellouin, N., Guttikunda, S. K., Hopke, P. K., Jacobson, M. Z., Kaiser, J. W., Klimont, Z., Lohmann, U., Schwarz, J. P., Shindell, D., Storelvmo, T., Warren, S. G. and Zender, C. S.: Bounding the role of black carbon in the climate system: A scientific assessment, J. Geophys. Res. Atmos., 118(11), 5380–5552, doi:10.1002/jgrd.50171, 2013.

Brandt, R. E., Warren, S. G. and Clarke, A. D.: A controlled snowmaking experiment testing the relation between black carbon content and reduction of snow albedo, J. Geophys. Res. Atmos., 116(8), doi:10.1029/2010JD015330, 2011.

Brown, R. D. and Robinson, D. A.: Northern Hemisphere spring snow cover variability and change over 1922-2010 including an assessment of uncertainty, Cryosphere, 5(1), 219–229, doi:10.5194/tc-5-219-2011, 2011.

Campanelli, M., Estellés, V., Tomasi, C., Nakajima, T., Malvestuto, V. and Martínez-Lozano, J. A.: Application of the SKYRAD Improved Langley plot method for the in situ calibration of CIMEL Sun-sky photometers., Appl. Opt., 46(14), 2688–702, doi:10.1364/AO.46.002688, 2007.

Chapman, E. G., Gustafson, W. I., Easter, R. C., Barnard, J. C., Ghan, S. J., Pekour, M. S. and Fast, J. D.: Coupling aerosol-cloud-radiative processes in the WRF-Chem model: Investigating the radiative impact of elevated point sources, Atmos. Chem. Phys., 9(3), 945–964, doi:10.5194/acp-9-945-2009, 2009.

Conway, H., Gades, A. and Raymond, C. F.: Albedo of dirty snow during conditions of melt, Water Resour. Res., 32(6), 1713–1718, doi:10.1029/96WR00712, 1996.

Dang, C., Fu, Q. and Warren, S. G.: Effect of Snow Grain Shape on Snow Albedo, J. Atmos. Sci., 73(9), 3573–3583, doi:10.1175/JAS-D-15-0276.1, 2016.

Dang, C., Warren, S. G., Fu, Q., Doherty, S. J., Sturm, M. and Su, J.: Measurements of light-

absorbing particles in snow across the Arctic, North America, and China: Effects on surface albedo, J. Geophys. Res. Atmos., 122(19), 10149–10168, doi:10.1002/2017JD027070, 2017.

Dentener, F., Kinne, S., Bond, T., Boucher, O., Cofala, J., Generoso, S., Ginoux, P., Gong, S., Hoelzemann, J. J., Ito, A., Marelli, L., Penner, J. E., Putaud, J. P., Textor, C., Schulz, M., Van Der Werf, G. R. and Wilson, J.: Emissions of primary aerosol and precursor gases in the years 2000 and 1750 prescribed data-sets for AeroCom, Atmos. Chem. Phys., 6(12), 4321–4344, doi:10.5194/acp-6-4321-2006, 2006.

Doherty, S. J., Warren, S. G., Grenfell, T. C., Clarke, A. D. and Brandt, R. E.: Light-absorbing impurities in Arctic snow, Atmos. Chem. Phys., 10(23), 11647–11680, doi:10.5194/acp-10-11647-2010, 2010.

Doherty, S. J., Grenfell, T. C., Forsström, S., Hegg, D. L., Brandt, R. E. and Warren, S. G.: Observed vertical redistribution of black carbon and other insoluble light-absorbing particles in melting snow, J. Geophys. Res. Atmos., 118(11), 5553–5569, doi:10.1002/jgrd.50235, 2013.

Dozier, J., Painter, T. H., Rittger, K. and Frew, J. E.: Time-space continuity of daily maps of fractional snow cover and albedo from MODIS, Adv. Water Resour., 31(11), 1515–1526, doi:10.1016/j.advwatres.2008.08.011, 2008.

Dubovik, O., Smirnov, A., Holben, B. N., King, M. D., Kaufman, Y. J., Eck, T. F. and Slutsker, I.: Accuracy assessments of aerosol optical properties retrieved from Aerosol Robotic Network (AERONET) Sun and sky radiance measurements, J. Geophys. Res. Atmos., 105(D8), 9791–9806, doi:10.1029/2000JD900040, 2000.

Dumka, U. C., Kaskaoutis, D. G., Srivastava, M. K. and Devara, P. C. S.: Scattering and absorption properties of near-surface aerosol over Gangetic-Himalayan region: The role of boundary-layer dynamics and long-range transport, Atmos. Chem. Phys., 15(3), 1555–1572, doi:10.5194/acp-15-1555-2015, 2015.

Dyurgerov, M. B.: Mountain glaciers at the end of the twentieth century: Global analysis in relation to climate and water cycle, Polar Geogr., 25(4), 241–336, doi:10.1080/10889370109377717, 2001.

Easter, R. C., Ghan, S. J., Zhang, Y., Saylor, R. D., Chapman, E. G., Laulainen, N. S., Abdul-Razzak, H., Leung, L. R., Bian, X. and Zaveri, R. A.: MIRAGE: Model description and evaluation of aerosols and trace gases, J. Geophys. Res. D Atmos., 109(20), doi:10.1029/2004JD004571, 2004.

Fan, J., Wang, Y., Rosenfeld, D. and Liu, X.: Review of Aerosol–Cloud Interactions: Mechanisms, Significance, and Challenges, J. Atmos. Sci., 73(11), 4221–4252, doi:10.1175/JAS-D-16-0037.1, 2016.

Fast, J. D., Gustafson, W. I., Easter, R. C., Zaveri, R. A., Barnard, J. C., Chapman, E. G., Grell, G. A. and Peckham, S. E.: Evolution of ozone, particulates, and aerosol direct radiative forcing in the vicinity of Houston using a fully coupled meteorology-chemistry-aerosol model, J. Geophys. Res. Atmos., 111(21), doi:10.1029/2005JD006721, 2006.

Flanner, M. G. and Zender, C. S.: Snowpack radiative heating: Influence on Tibetan Plateau climate, Geophys. Res. Lett., 32(6), 1–5, doi:10.1029/2004GL022076, 2005.

Flanner, M. G., Zender, C. S., Randerson, J. T. and Rasch, P. J.: Present-day climate forcing and response from black carbon in snow, J. Geophys. Res. Atmos., 112(11), doi:10.1029/2006JD008003, 2007.

Flanner, M. G., Zender, C. S., Hess, P. G., Mahowald, N. M., Painter, T. H., Ramanathan, V. and Rasch, P. J.: Springtime warming and reduced snow cover from carbonaceous particles, Atmos. Chem. Phys., 9(7), 2481–2497, doi:10.5194/acp-9-2481-2009, 2009.

Flanner, M. G., Liu, X., Zhou, C., Penner, J. E. and Jiao, C.: Enhanced solar energy absorption by internally-mixed black carbon in snow grains, Atmos. Chem. Phys., 12(10), 4699–4721, doi:10.5194/acp-12-4699-2012, 2012.

Gautam, R., Hsu, N. C., Lau, W. K. M. and Yasunari, T. J.: Satellite observations of desert dust-induced Himalayan snow darkening, Geophys. Res. Lett., 40(5), 988–993, doi:10.1002/grl.50226, 2013.

Gertler, C. G., Puppala, S. P., Panday, A., Stumm, D. and Shea, J.: Black carbon and the Himalayan cryosphere: A review, Atmos. Environ., 125, 404–417, doi:10.1016/j.atmosenv.2015.08.078, 2016.

Ghatak, D., Sinsky, E. and Miller, J.: Role of snow-albedo feedback in higher elevation warming over the Himalayas, Tibetan Plateau and Central Asia, Environ. Res. Lett., 9(11), doi:10.1088/1748-9326/9/11/114008, 2014.

Ginot, P., Dumont, M., Lim, S., Patris, N., Taupin, J. D., Wagnon, P., Gilbert, A., Arnaud, Y., Marinoni, A., Bonasoni, P. and Laj, P.: A 10 year record of black carbon and dust from a Mera Peak ice core (Nepal): Variability and potential impact on melting of Himalayan glaciers, Cryosphere, 8(4), 1479–1496, doi:10.5194/tc-8-1479-2014, 2014.

Ginoux, P., Chin, M., Tegen, I., Prospero, J. M., Holben, B., Dubovik, O. and Lin, S.-J.: Sources and distributions of dust aerosols simulated with the GOCART model, J. Geophys. Res. Atmos., 106(D17), 20255–20273, doi:10.1029/2000JD000053, 2001.

Gustafson, W. I., Chapman, E. G., Ghan, S. J., Easter, R. C. and Fast, J. D.: Impact on modeled cloud characteristics due to simplified treatment of uniform cloud condensation nuclei during NEAQS 2004, Geophys. Res. Lett., 34(19), doi:10.1029/2007GL030021, 2007.

Hadley, O. L. and Kirchstetter, T. W.: Black-carbon reduction of snow albedo, Nat. Clim. Chang., 2(6), 437–440, doi:10.1038/nclimate1433, 2012.

Hansen, J. and Nazarenko, L.: Soot climate forcing via snow and ice albedos, Proc. Natl. Acad. Sci., 101(2), 423–428, doi:10.1073/pnas.2237157100, 2004.

Hansen, J., Sato, M. and Ruedy, R.: Radiative forcing and climate response, J. Geophys. Res. Atmos., 102(D6), 6831–6864, doi:10.1029/96JD03436, 1997.

He, C., Takano, Y., Liou, K.-N., Yang, P., Li, Q. and Chen, F.: Impact of Snow Grain Shape and Black Carbon–Snow Internal Mixing on Snow Optical Properties: Parameterizations for Climate Models, J. Clim., 30(24), 10019–10036, doi:10.1175/JCLI-D-17-0300.1, 2017.

He, C., Flanner, M. G., Chen, F., Barlage, M., Liou, K. N., Kang, S., Ming, J. and Qian, Y.: Black carbon-induced snow albedo reduction over the Tibetan Plateau: Uncertainties from snow

grain shape and aerosol-snow mixing state based on an updated SNICAR model, Atmos. Chem. Phys., 18(15), 11507–11527, doi:10.5194/acp-18-11507-2018, 2018.

Hess, M., Koepke, P. and Schult, I.: Optical Properties of Aerosols and Clouds: The Software Package OPAC, Bull. Am. Meteorol. Soc., 79(5), 831–844, doi:10.1175/1520-0477(1998)079<0831:OPOAAC>2.0.CO;2, 1998.

Holben, B. N., Eck, T. F., Slutsker, I., Tanré, D., Buis, J. P., Setzer, A., Vermote, E., Reagan, J. A., Kaufman, Y. J., Nakajima, T., Lavenu, F., Jankowiak, I. and Smirnov, A.: AERONET—A Federated Instrument Network and Data Archive for Aerosol Characterization, Remote Sens. Environ., 66(1), 1–16, doi:10.1016/S0034-4257(98)00031-5, 1998.

Hu, Z., Zhao, C., Huang, J., Leung, L. R., Qian, Y., Yu, H., Huang, L. and Kalashnikova, O. V.: Trans-Pacific transport and evolution of aerosols: Evaluation of quasi-global WRF-Chem simulation with multiple observations, Geosci. Model Dev., 9(5), 1725–1746, doi:10.5194/gmd-9-1725-2016, 2016.

Immerzeel, W. W., Van Beek, L. P. H. and Bierkens, M. F. P.: Climate change will affect the asian water towers, Science (80-.)., 328(5984), 1382–1385, doi:10.1126/science.1183188, 2010.

IPCC: Climate change 2013: The physical science basis, Contrib. Work. Gr. I to Fifth Assess. Rep. Intergov. Panel Clim. Chang., 33, doi:10.1017/CBO9781107415324, 2013.

Jacobi, H. W., Lim, S., Ménégoz, M., Ginot, P., Laj, P., Bonasoni, P., Stocchi, P., Marinoni, A. and Arnaud, Y.: Black carbon in snow in the upper Himalayan Khumbu Valley, Nepal: Observations and modeling of the impact on snow albedo, melting, and radiative forcing, Cryosphere, 9(4), 1685–1699, doi:10.5194/tc-9-1685-2015, 2015.

Jayarathne, T., Stockwell, C. E., Bhave, P. V., Praveen, P. S., Rathnayake, C. M., Md Islam, R., Panday, A. K., Adhikari, S., Maharjan, R., Douglas Goetz, J., Decarlo, P. F., Saikawa, E., Yokelson, R. J. and Stone, E. A.: Nepal Ambient Monitoring and Source Testing Experiment (NAMaSTE): Emissions of particulate matter from wood-and dung-fueled cooking fires, garbage and crop residue burning, brick kilns, and other sources, Atmos. Chem. Phys., 18(3), 2259–2286, doi:10.5194/acp-18-2259-2018, 2018.

Ji, Z. M.: Modeling black carbon and its potential radiative effects over the Tibetan Plateau, Adv. Clim. Chang. Res., 7(3), 139–144, doi:10.1016/j.accre.2016.10.002, 2016.

Kaser, G., Grosshauser, M. and Marzeion, B.: Contribution potential of glaciers to water availability in different climate regimes, Proc. Natl. Acad. Sci., 107(47), 20223–20227, doi:10.1073/pnas.1008162107, 2010.

Kaspari, S., Painter, T. H., Gysel, M., Skiles, S. M. and Schwikowski, M.: Seasonal and elevational variations of black carbon and dust in snow and ice in the Solu-Khumbu, Nepal and estimated radiative forcings, Atmos. Chem. Phys., 14(15), 8089–8103, doi:10.5194/acp-14-8089-2014, 2014.

Khan, A. A., Pant, N. C., Sarkar, A., Tandon, S. K., Thamban, M. and Mahalinganathan, K.: The Himalayan cryosphere: A critical assessment and evaluation of glacial melt fraction in the Bhagirathi basin, Geosci. Front., 8(1), 107–115, doi:10.1016/j.gsf.2015.12.009, 2017.

Kopacz, M., Mauzerall, D. L., Wang, J., Leibensperger, E. M., Henze, D. K. and Singh, K.:

Origin and radiative forcing of black carbon transported to the Himalayas and Tibetan Plateau, Atmos. Chem. Phys., 11(6), 2837–2852, doi:10.5194/acp-11-2837-2011, 2011.

Kulkarni, A. V., Rathore, B. P. and Singh, S. K.: Distribution of seasonal snow cover in central and western Himalaya, Ann. Glaciol., 51(54), 123–128, doi:10.3189/172756410791386445, 2010.

Lau, K. M., Kim, M. K. and Kim, K. M.: Asian summer monsoon anomalies induced by aerosol direct forcing: The role of the Tibetan Plateau, Clim. Dyn., 26(7–8), 855–864, doi:10.1007/s00382-006-0114-z, 2006.

Lau, W. K. M., Kim, M. K., Kim, K. M. and Lee, W. S.: Enhanced surface warming and accelerated snow melt in the Himalayas and Tibetan Plateau induced by absorbing aerosols, Environ. Res. Lett., 5(2), doi:10.1088/1748-9326/5/2/025204, 2010.

Levy, R. C., Remer, L. A., Mattoo, S., Vermote, E. F. and Kaufman, Y. J.: Second-generation operational algorithm: Retrieval of aerosol properties over land from inversion of Moderate Resolution Imaging Spectroradiometer spectral reflectance, J. Geophys. Res. Atmos., 112(13), doi:10.1029/2006JD007811, 2007.

Levy, R. C., Remer, L. A., Kleidman, R. G., Mattoo, S., Ichoku, C., Kahn, R. and Eck, T. F.: Global evaluation of the Collection 5 MODIS dark-target aerosol products over land, Atmos. Chem. Phys., 10(21), 10399–10420, doi:10.5194/acp-10-10399-2010, 2010.

Li, Z., Lau, W. K. M., Ramanathan, V., Wu, G., Ding, Y., Manoj, M. G., Liu, J., Qian, Y., Li, J., Zhou, T., Fan, J., Rosenfeld, D., Ming, Y., Wang, Y., Huang, J., Wang, B., Xu, X., Lee, S. S., Cribb, M., Zhang, F., Yang, X., Zhao, C., Takemura, T., Wang, K., Xia, X., Yin, Y., Zhang, H., Guo, J., Zhai, P. M., Sugimoto, N., Babu, S. S. and Brasseur, G. P.: Aerosol and monsoon climate interactions over Asia, Rev. Geophys., 54(4), 866–929, doi:10.1002/2015RG000500, 2016.

Liou, K. N., Takano, Y., He, C., Yang, P., Leung, L. R., Gu, Y. and Lee, W. L.: Stochastic parameterization for light absorption by internally mixed BC/dust in snow grains for application to climate models, J. Geophys. Res. Atmos., 119(12), 7616–7632, doi:10.1002/2014JD021665, 2014.

Marcq, S., Laj, P., Roger, J. C., Villani, P., Sellegri, K., Bonasoni, P., Marinoni, A., Cristofanelli, P., Verza, G. P. and Bergin, M.: Aerosol optical properties and radiative forcing in the high Himalaya based on measurements at the Nepal Climate Observatory-Pyramid site (5079 m a.s.l.), Atmos. Chem. Phys., 10(13), 5859–5872, doi:10.5194/acp-10-5859-2010, 2010.

Ménégoz, M., Krinner, G., Balkanski, Y., Boucher, O., Cozic, A., Lim, S., Ginot, P., Laj, P., Gallée, H., Wagnon, P., Marinoni, A. and Jacobi, H. W.: Snow cover sensitivity to black carbon deposition in the Himalayas: From atmospheric and ice core measurements to regional climate simulations, Atmos. Chem. Phys., 14(8), 4237–4249, doi:10.5194/acp-14-4237-2014, 2014.

Menon, S., Koch, D., Beig, G., Sahu, S., Fasullo, J. and Orlikowski, D.: Black carbon aerosols and the third polar ice cap, Atmos. Chem. Phys., 10(10), 4559–4571, doi:10.5194/acp-10-4559-2010, 2010.

Ming, J., Cachier, H., Xiao, C., Qin, D., Kang, S., Hou, S. and Xu, J.: Black carbon record based

on a shallow Himalayan ice core and its climatic implications, Atmos. Chem. Phys., 8(5), 1343–1352, doi:10.5194/acp-8-1343-2008, 2008.

Mlawer, E. J., Taubman, S. J., Brown, P. D., Iacono, M. J. and Clough, S. A.: Radiative transfer for inhomogeneous atmospheres: RRTM, a validated correlated-k model for the longwave, J. Geophys. Res. Atmos., 102(D14), 16663–16682, doi:10.1029/97JD00237, 1997.

Nair, V. S., Babu, S. S., Moorthy, K. K., Sharma, A. K., Marinoni, A. and Ajai: Black carbon aerosols over the Himalayas: Direct and surface albedo forcing, Tellus, Ser. B Chem. Phys. Meteorol., 65(1), doi:10.3402/tellusb.v65i0.19738, 2013.

Nakajima, T., Tonna, G., Rao, R., Boi, P., Kaufman, Y. and Holben, B.: Use of sky brightness measurements from ground for remote sensing of particulate polydispersions, Appl. Opt., 35(15), 2672, doi:10.1364/AO.35.002672, 1996.

Ningombam, S. S., Srivastava, A. K., Bagare, S. P., Singh, R. B., Kanawade, V. P. and Dorjey, N.: Assessment of aerosol optical and micro-physical features retrieved from direct and diffuse solar irradiance measurements from Skyradiometer at a high altitude station at Merak: Assessment of aerosol optical features from Merak, Environ. Sci. Pollut. Res., 22(21), 16610–16619, doi:10.1007/s11356-015-4788-9, 2015.

Niu, H., Kang, S., Wang, H., Zhang, R., Lu, X., Qian, Y., Paudyal, R., Wang, S., Shi, X. and Yan, X.: Seasonal variation and light absorption property of carbonaceous aerosol in a typical glacier region of the southeastern Tibetan Plateau, Atmos. Chem. Phys., 18(9), 6441–6460, doi:10.5194/acp-18-6441-2018, 2018.

Oleson, K. W., Lawrence, D. M., Gordon, B., Flanner, M. G., Kluzek, E., Peter, J., Levis, S., Swenson, S. C., Thornton, E. and Feddema, J.: Technical description of version 4.0 of the Community Land Model (CLM)., 2010.

Painter, T. H., Rittger, K., McKenzie, C., Slaughter, P., Davis, R. E. and Dozier, J.: Retrieval of subpixel snow covered area, grain size, and albedo from MODIS, Remote Sens. Environ., 113(4), 868–879, doi:10.1016/j.rse.2009.01.001, 2009.

Painter, T. H., Bryant, A. C. and McKenzie Skiles, S.: Radiative forcing by light absorbing impurities in snow from MODIS surface reflectance data, Geophys. Res. Lett., 39(17), doi:10.1029/2012GL052457, 2012.

Painter, T. H., Seidel, F. C., Bryant, A. C., McKenzie Skiles, S. and Rittger, K.: Imaging spectroscopy of albedo and radiative forcing by light-absorbing impurities in mountain snow, J. Geophys. Res. Atmos., 118(17), 9511–9523, doi:10.1002/jgrd.50520, 2013.

Pfeffer, W. T., Arendt, A. A., Bliss, A., Bolch, T., Cogley, J. G., Gardner, A. S., Hagen, J. O., Hock, R., Kaser, G., Kienholz, C., Miles, E. S., Moholdt, G., Mölg, N., Paul, F., Radić, V., Rastner, P., Raup, B. H., Rich, J., Sharp, M. J., Andreassen, L. M., Bajracharya, S., Barrand, N. E., Beedle, M. J., Berthier, E., Bhambri, R., Brown, I., Burgess, D. O., Burgess, E. W., Cawkwell, F., Chinn, T., Copland, L., Cullen, N. J., Davies, B., De Angelis, H., Fountain, A. G., Frey, H., Giffen, B. A., Glasser, N. F., Gurney, S. D., Hagg, W., Hall, D. K., Haritashya, U. K., Hartmann, G., Herreid, S., Howat, I., Jiskoot, H., Khromova, T. E., Klein, A., Kohler, J., König, M., Kriegel, D., Kutuzov, S., Lavrentiev, I., Le Bris, R., Li, X., Manley, W. F., Mayer, C., Menounos, B., Mercer, A., Mool, P., Negrete, A., Nosenko, G., Nuth, C., Osmonov, A.,

Pettersson, R., Racoviteanu, A., Ranzi, R., Sarikaya, M. A., Schneider, C., Sigurdsson, O., Sirguey, P., Stokes, C. R., Wheate, R., Wolken, G. J., Wu, L. Z. and Wyatt, F. R.: The randolph glacier inventory: A globally complete inventory of glaciers, J. Glaciol., 60(221), 537–552, doi:10.3189/2014JoG13J176, 2014.

Prasad, A. K., S. Yang, K. H., El-Askary, H. M. and Kafatos, M.: Melting of major Glaciers in the western Himalayas: Evidence of climatic changes from long term MSU derived tropospheric temperature trend (1979-2008), Ann. Geophys., 27(12), 4505–4519, doi:10.5194/angeo-27-4505-2009, 2009.

Qian, Y., Gong, D., Fan, J., Ruby Leung, L., Bennartz, R., Chen, D. and Wang, W.: Heavy pollution suppresses light rain in China: Observations and modeling, J. Geophys. Res. Atmos., 114(15), doi:10.1029/2008JD011575, 2009.

Qian, Y., Flanner, M. G., Leung, L. R. and Wang, W.: Sensitivity studies on the impacts of Tibetan Plateau snowpack pollution on the Asian hydrological cycle and monsoon climate, Atmos. Chem. Phys., 11(5), 1929–1948, doi:10.5194/acp-11-1929-2011, 2011.

Qian, Y., Wang, H., Zhang, R., Flanner, M. G. and Rasch, P. J.: A sensitivity study on modeling black carbon in snow and its radiative forcing over the Arctic and Northern China, Environ. Res. Lett., 9(6), doi:10.1088/1748-9326/9/6/064001, 2014.

Qian, Y., Yasunari, T. J., Doherty, S. J., Flanner, M. G., Lau, W. K. M., Ming, J., Wang, H., Wang, M., Warren, S. G. and Zhang, R.: Light-absorbing particles in snow and ice: Measurement and modeling of climatic and hydrological impact, Adv. Atmos. Sci., 32(1), 64–91, doi:10.1007/s00376-014-0010-0, 2015.

Raatikainen, T., Hyvärinen, A. P., Hatakka, J., Panwar, T. S., Hooda, R. K., Sharma, V. P. and Lihavainen, H.: The effect of boundary layer dynamics on aerosol properties at the Indo-Gangetic plains and at the foothills of the Himalayas, Atmos. Environ., 89, 548–555, doi:10.1016/j.atmosenv.2014.02.058, 2014.

V. Ramanathan and G. Carmichael: Global and regional climate changes due to black carbon, Nat. Geosci., 1(January), 221–227, doi:10.1038/ngeo156, 2008.

Ramanathan, V., Crutzen, P. J., Kiehl, J. T., Rosenfeld, D., Haywood, J., Boucher, O., Kaufman, Y. J., Collins, W. D., Hansen, J. E., Sato, M., Ruedy, R., Kiehl, J. T., Trenberth, K. E., Crutzen, P. J., Andreae, M. O., Charlson, R. J., Langner, J., Rodhe, H., Leovy, C. B., Warren, S. G., Clarke, A. D., Charlson, R. J., Grassl, H., Ogren, J. A., Charlson, R. J., Jayaraman, A., Satheesh, S. K., Ramanathan, V., Jacobson, M. J., Russell, P. B., Eck, T. F., Holben, B. N., Slutsker, I., Setzer, A., Raes, F., Bates, T., McGovern, F., Liedekerke, M. Van, Rajeev, K., Ramanathan, V., Meywerk, J., Lelieveld, J., Ramanathan, V., Konzelmann, T., Cahoon, D. R., Whitlock, C. H., Twomey, S., Novakov, T., Penner, J. E., Charlson, R. J., Martin, G. M., Johnson, W., Spice, A., Guiltepe, I., Issac, G. A., Leaitch, W. R., Banic, C. M., Pawlowska, H., Brenguier, J.-L., Taylor, J. P., McHafffie, A., Coakley, J. A., Bernstein, R. L., Durkey, P. A., Kaufman, Y. J., Fraser, R. S., Nakajima, T., Higurashi, A., Kawamoto, K., Penner, J. E., Hansen, J., Sato, M., Ruedy, R., Lacis, A., Oinas, V., Warner, J. J., Rosenfeld, D., ___., ___., Rudich, Y., Lahav, R., Levitus, S., Stanhill, G., Cohen, S., Gilgen, H., Wild, M., Ohmura, A., Ramaswamy, V., Chen, C. T., Meehl, G. A., Washington, W. M., Erickson, D. J., Briegleb, B. P., Jaumann, P. J., Michell, J. F. B., Johns, T. C., Roeckner, E., Bengtsson, L., Feichter, J., et al.: Aerosols, climate, and the

hydrological cycle., Science, 294(5549), 2119–24, doi:10.1126/science.1064034, 2001.

Ramanathan, V., Ramana, M. V., Roberts, G., Kim, D., Corrigan, C., Chung, C. and Winker, D.: Warming trends in Asia amplified by brown cloud solar absorption, Nature, 448(7153), 575–578, doi:10.1038/nature06019, 2007.

Ren, D. and Karoly, D.: Comparison of glacier-inferred temperatures with observations and climate model simulations, Geophys. Res. Lett., 33(23), doi:10.1029/2006GL027856, 2006.

Ren, J., Jing, Z., Pu, J. and Qin, X.: Glacier variations and climate change in the central Himalaya over the past few decades, in Annals of Glaciology, vol. 43, pp. 218–222., 2006.

Rittger, K., Painter, T. H. and Dozier, J.: Assessment of methods for mapping snow cover from MODIS, Adv. Water Resour., 51, 367–380, doi:10.1016/j.advwatres.2012.03.002, 2013.

Rittger, K., Bair, E. H., Kahl, A. and Dozier, J.: Spatial estimates of snow water equivalent from reconstruction, Adv. Water Resour., 94, 345–363, doi:10.1016/j.advwatres.2016.05.015, 2016.

Sarangi, C., Tripathi, S. N., Kanawade, V. P., Koren, I. and Sivanand Pai, D.: Investigation of the aerosol-cloud-rainfall association over the Indian summer monsoon region, Atmos. Chem. Phys., 17(8), doi:10.5194/acp-17-5185-2017, 2017.

Schmale, J., Flanner, M., Kang, S., Sprenger, M., Zhang, Q., Guo, J., Li, Y., Schwikowski, M. and Farinotti, D.: Modulation of snow reflectance and snowmelt from Central Asian glaciers by anthropogenic black carbon, Sci. Rep., 7, doi:10.1038/srep40501, 2017.

Shrestha, A. B., Wake, C. P., Mayewski, P. A. and Dibb, J. E.: Maximum temperature trends in the Himalaya and its vicinity: An analysis based on temperature records from Nepal for the period 1971-94, J. Clim., 12(9), 2775–2786, doi:10.1175/1520-0442(1999)012<2775:MTTITH>2.0.CO;2, 1999.

Simard, M., Pinto, N., Fisher, J. B. and Baccini, A.: Mapping forest canopy height globally with spaceborne lidar, J. Geophys. Res. Biogeosciences, 116(4), doi:10.1029/2011JG001708, 2011.

Singh, P. and Bengtsson, L.: Hydrological sensitivity of a large Himalayan basin to climate change, Hydrol. Process., 18(13), 2363–2385, doi:10.1002/hyp.1468, 2004.

Skiles, S. M., Painter, T. H., Deems, J. S., Bryant, A. C. and Landry, C. C.: Dust radiative forcing in snow of the Upper Colorado River Basin: 2. Interannual variability in radiative forcing and snowmelt rates, Water Resour. Res., 48(7), doi:10.1029/2012WR011986, 2012.

Skiles, S. M., Painter, T. H., Belnap, J., Holland, L., Reynolds, R. L., Goldstein, H. L. and Lin, J.: Regional variability in dust-on-snow processes and impacts in the Upper Colorado River Basin, Hydrol. Process., 29(26), 5397–5413, doi:10.1002/hyp.10569, 2015.

Skiles, S. M. K. and Painter, T.: Daily evolution in dust and black carbon content, snow grain size, and snow albedo during snowmelt, Rocky Mountains, Colorado, J. Glaciol., 63(237), 118–132, doi:10.1017/jog.2016.125, 2017.

Svensson, J., Ström, J., Kivekäs, N., Dkhar, N. B., Tayal, S., Sharma, V. P., Jutila, A., Backman, J., Virkkula, A., Ruppel, M., Hyvärinen, A., Kontu, A., Backman, J., Leppäranta, M., Hooda, R. K., Korhola, A., Asmi, E. and Lihavainen, H.: Light-Absorption of dust and elemental carbon in

snow in the Indian Himalayas and the Finnish Arctic, Atmos. Meas. Tech., 11(3), 1403–1416, doi:10.5194/amt-11-1403-2018, 2018.

Toon, O. B., McKay, C. P., Ackerman, T. P. and Santhanam, K.: Rapid calculation of radiative heating rates and photodissociation rates in inhomogeneous multiple scattering atmospheres, J. Geophys. Res., 94(D13), 16287, doi:10.1029/JD094iD13p16287, 1989.

Tripathi, S. N., Dey, S., Chandel, A., Srivastava, S., Singh, R. P. and Holben, B. N.: Comparison of MODIS and AERONET derived aerosol optical depth over the Ganga Basin, India, Ann. Geophys., 23(4), 1093–1101, doi:10.5194/angeo-23-1093-2005, 2005.

Wake, C. P., Mayewski, P. A., Li, Z., Han, J. and Qin, D.: Modern eolian dust deposition in central Asia, Tellus B Chem. Phys. Meteorol., 46(3), 220–233, doi:10.3402/tellusb.v46i3.15793, 1994.

Wang, B., Bao, Q., Hoskins, B., Wu, G. and Liu, Y.: Tibetan Plateau warming and precipitation changes in East Asia, Geophys. Res. Lett., 35(14), doi:10.1029/2008GL034330, 2008.

Wang, M., Xu, B., Cao, J., Tie, X., Wang, H., Zhang, R., Qian, Y., Rasch, P. J., Zhao, S., Wu, G., Zhao, H., Joswiak, D. R., Li, J. and Xie, Y.: Carbonaceous aerosols recorded in a southeastern Tibetan glacier: Analysis of temporal variations and model estimates of sources and radiative forcing, Atmos. Chem. Phys., 15(3), 1191–1204, doi:10.5194/acp-15-1191-2015, 2015a.

Wang, M., Xu, B., Kaspari, S. D., Gleixner, G., Schwab, V. F., Zhao, H., Wang, H. and Yao, P.: Century-long record of black carbon in an ice core from the Eastern Pamirs: Estimated contributions from biomass burning, Atmos. Environ., 115, 79–88, doi:10.1016/j.atmosenv.2015.05.034, 2015b.

Warren, S. G.: Can black carbon in snow be detected by remote sensing?, J. Geophys. Res. Atmos., 118(2), 779–786, doi:10.1029/2012JD018476, 2013.

Warren, S. G. and Wiscombe, W. J.: A Model for the Spectral Albedo of Snow. II: Snow Containing Atmospheric Aerosols, J. Atmos. Sci., 37(12), 2734–2745, doi:10.1175/1520-0469(1980)037<2734:AMFTSA>2.0.CO;2, 1980.

Van Der Werf, G. R., Randerson, J. T., Giglio, L., Collatz, G. J., Mu, M., Kasibhatla, P. S., Morton, D. C., Defries, R. S., Jin, Y. and Van Leeuwen, T. T.: Global fire emissions and the contribution of deforestation, savanna, forest, agricultural, and peat fires (1997-2009), Atmos. Chem. Phys., 10(23), 11707–11735, doi:10.5194/acp-10-11707-2010, 2010.

Xu, B., Cao, J., Hansen, J., Yao, T., Joswia, D. R., Wang, N., Wu, G., Wang, M., Zhao, H., Yang, W., Liu, X. and He, J.: Black soot and the survival of Tibetan glaciers, Proc. Natl. Acad. Sci., 106(52), 22114–22118, doi:10.1073/pnas.0910444106, 2009a.

Xu, J., Grumbine, R. E., Shrestha, A., Eriksson, M., Yang, X., Wang, Y. and Wilkes, A.: The melting Himalayas: Cascading effects of climate change on water, biodiversity, and livelihoods, Conserv. Biol., 23(3), 520–530, doi:10.1111/j.1523-1739.2009.01237.x, 2009b.

Yao, T., Pu, J., Lu, A., Wang, Y. and Yu, W.: Recent Glacial Retreat and Its Impact on Hydrological Processes on the Tibetan Plateau, China, and Surrounding Regions, Arctic, Antarct. Alp. Res., 39(4), 642–650, doi:10.1657/1523-0430(07-510)[YAO]2.0.CO;2, 2007.

Yasunari, T. J., Bonasoni, P., Laj, P., Fujita, K., Vuillermoz, E., Marinoni, A., Cristofanelli, P., Duchi, R., Tartari, G. and Lau, K. M.: Estimated impact of black carbon deposition during pre-monsoon season from Nepal Climate Observatory - Pyramid data and snow albedo changes over Himalayan glaciers, Atmos. Chem. Phys., 10(14), 6603–6615, doi:10.5194/acp-10-6603-2010, 2010a.

Yasunari, T. J., Bonasoni, P., Laj, P., Fujita, K., Vuillermoz, E., Marinoni, A., Cristofanelli, P., Duchi, R., Tartari, G. and Lau, K.-M.: Preliminary estimation of black carbon deposition from Nepal Climate Observatory-Pyramid data and its possible impact on snow albedo changes over Himalayan glaciers during the pre-monsoon season., Atmos. Chem. Phys. Discuss., 10(4), 9291–9328 [online] Available from: https://ezp.lib.unimelb.edu.au/login?url=https://search.ebscohost.com/login.aspx?direct=true&db=eih&AN=51503391&site=eds-live&scope=site, 2010b.

Yasunari, T. J., Tan, Q., Lau, K. M., Bonasoni, P., Marinoni, A., Laj, P., Ménégoz, M., Takemura, T. and Chin, M.: Estimated range of black carbon dry deposition and the related snow albedo reduction over Himalayan glaciers during dry pre-monsoon periods, Atmos. Environ., 78, 259–267, doi:10.1016/j.atmosenv.2012.03.031, 2013.

Zaveri, R. A. and Peters, L. K.: A new lumped structure photochemical mechanism for large-scale applications, J. Geophys. Res. Atmos., 104(D23), 30387–30415, doi:10.1029/1999JD900876, 1999.

Zaveri, R. A., Easter, R. C., Fast, J. D. and Peters, L. K.: Model for Simulating Aerosol Interactions and Chemistry (MOSAIC), J. Geophys. Res. Atmos., 113(13), doi:10.1029/2007JD008782, 2008.

Zhang, Q., Streets, D. G., Carmichael, G. R., He, K. B., Huo, H., Kannari, A., Klimont, Z., Park, I. S., Reddy, S., Fu, J. S., Chen, D., Duan, L., Lei, Y., Wang, L. T. and Yao, Z. L.: Asian emissions in 2006 for the NASA INTEX-B mission, Atmos. Chem. Phys., 9(14), 5131–5153, doi:10.5194/acp-9-5131-2009, 2009.

Zhang, R., Wang, H., Qian, Y., Rasch, P. J., Easter, R. C., Ma, P. L., Singh, B., Huang, J. and Fu, Q.: Quantifying sources, transport, deposition, and radiative forcing of black carbon over the Himalayas and Tibetan Plateau, Atmos. Chem. Phys., 15(11), 6205–6223, doi:10.5194/acp-15-6205-2015, 2015.

Zhang, Y., Kang, S., Sprenger, M., Cong, Z., Gao, T., Li, C., Tao, S., Li, X., Zhong, X., Xu, M., Meng, W., Neupane, B., Qin, X. and Sillanpää, M.: Black carbon and mineral dust in snow cover on the Tibetan Plateau, Cryosph., 12(2), 413–431, doi:10.5194/tc-12-413-2018, 2018.

Zhao, C., Liu, X., Leung, L. R. and Hagos, S.: Radiative impact of mineral dust on monsoon precipitation variability over West Africa, Atmos. Chem. Phys., 11(5), 1879–1893, doi:10.5194/acp-11-1879-2011, 2011.

Zhao, C., Leung, L. R., Easter, R., Hand, J. and Avise, J.: Characterization of speciated aerosol direct radiative forcing over California, J. Geophys. Res. Atmos., 118(5), 2372–2388, doi:10.1029/2012JD018364, 2013a.

Zhao, C., Chen, S., Leung, L. R., Qian, Y., Kok, J. F., Zaveri, R. A. and Huang, J.: Uncertainty in modeling dust mass balance and radiative forcing from size parameterization, Atmos. Chem.

Phys., 13(21), 10733–10753, doi:10.5194/acp-13-10733-2013, 2013b.

Zhao, C., Hu, Z., Qian, Y., Ruby Leung, L., Huang, J., Huang, M., Jin, J., Flanner, M. G., Zhang, R., Wang, H., Yan, H., Lu, Z. and Streets, D. G.: Simulating black carbon and dust and their radiative forcing in seasonal snow: A case study over North China with field campaign measurements, Atmos. Chem. Phys., 14(20), 11475–11491, doi:10.5194/acp-14-11475-2014, 2014.